

Regularization effects in the Nambu-Jona-Lasinio model: Strong scheme dependence of inhomogeneous phases and persistence of the moat regime

Laurin Pannullo^{1,*}, Marc Wagner^{2,3,†} and Marc Winstel^{2‡}

¹*Fakultät für Physik, Universität Bielefeld, Universitätsstraße 25, D-33615 Bielefeld, Germany.*

²*Institut für Theoretische Physik, Goethe Universität Frankfurt am Main,*

Max-von-Laue-Straße 1, D-60438 Frankfurt, Germany

³*Helmholtz Research Academy Hesse for FAIR, Campus Riedberg,*

Max-von-Laue-Straße 12, D-60438 Frankfurt, Germany

(Dated: June 18, 2024)

This work investigates the phase structure of the non-renormalizable (3+1)-dimensional Nambu-Jona-Lasinio (NJL) model with particular focus on inhomogeneous phases (IPs), where the chiral condensate is non-uniform in space, and the closely related moat regimes, where mesonic dispersion relations favor non-vanishing momenta. We use the mean-field approximation and consider five different regularization schemes including three lattice discretizations. The results within the different regularization schemes are systematically analyzed in order to study the dependence of the IP on the choice of regularization scheme and regulator value. The IP exhibits a drastic dependence on the chosen regularization scheme rendering any physical interpretation of results on inhomogeneous phases in this model doubtful. In contrast, we find only a mild scheme dependence of the moat regime suggesting that its existence is a consequence of the action of the NJL model and its symmetries and, thus, that it might also exist in QCD.

Keywords: Nambu-Jona-Lasinio model, stability analysis, inhomogeneous phases, moat regimes, regulator dependence, mean-field

I. INTRODUCTION

Inhomogeneous phases (IPs) are phases where in addition to chiral symmetry also translational invariance is broken, i.e., the chiral condensate $\langle \bar{\psi}\psi \rangle$ is a function of the spatial coordinates $\vec{x} = (x_1, x_2, x_3)$. An IP is one of several, not necessarily mutually exclusive scenarios which are considered to be relevant in the phase diagram of Quantum Chromodynamics (QCD) at non-vanishing chemical potential μ and low to intermediate temperature T . Other conjectured scenarios for the QCD phase diagram in that region include color-superconducting phases [1], quarkyonic matter [2, 3] or liquid-crystal like behavior [4, 5]. Phases with spatially modulated chiral currents, that are observed in holographic models fitted to lattice QCD data [6–10], could possibly coincide or be an alternative scenario to an IP.

While the phase diagram of QCD, is well understood for small chemical potentials from lattice simulations [11–14], the phase structure for intermediate and large chemical potentials is less clear and an active area of current research. A common scenario is that the crossover is replaced at some non-vanishing value for μ by a first-order transition starting at a critical endpoint (CP) and continuing down to zero temperature. Various functional methods predict this point at $\mu_{\text{cep}} > T_{\text{cep}}$ [15–17]. While these methods necessitate certain approximations, their predictions are supported by lattice results that determine the location of the CP by analyzing Lee-Yang zeros [18].

Moreover, similar findings are obtained when using QCD-inspired models such as the Nambu-Jona-Lasinio (NJL) model or the quark-meson model, see, e.g., Refs. [19, 20]. Due to the technical challenges for the lattice and functional methods at intermediate μ , e.g., the sign problem, the majority of the current QCD phase diagram predictions of a first order phase transition and a CP are based on QCD-inspired models.

The above described scenario is based on the assumption of exclusively homogeneous condensation. When allowing the condensates to depend on the spatial coordinates, the first-order phase transition between the homogeneously broken phase (HBP) and the symmetric phase (SP) is typically replaced and gets covered by an IP in NJL and quark-meson model calculations [21–25]. Often, the former CP is then replaced by a so-called Lifshitz point (LP), which coincides with the common end point of the two boundary lines of the IP [23–25]. Such model calculations have led to the conjecture that the IP might be a feature of the QCD phase diagram at non-vanishing μ and also at large magnetic fields [26–28].

Apart from model investigations there is also evidence from functional approaches supporting this conjecture. Studies employing a Dyson-Schwinger approach to QCD have shown that an IP is a self-consistent solution in the QCD phase diagram [29] and instabilities of a chirally symmetric solution towards an inhomogeneous condensate exist [30, 31]. Also, investigations using the Functional Renormalization Group [16] support the existence of a moat regime in QCD, a regime with an exotic meson dispersion relation featuring a minimum at non-vanishing momentum [32]. It is argued that this moat dispersion relation is a precursor to an IP, since it favors particles with non-vanishing momenta. Indeed, the moat disper-

* lpanullo@physik.uni-bielefeld.de

† mwagner@itp.uni-frankfurt.de

‡ winstel@itp.uni-frankfurt.de

sion relation was recently shown to coincide with large parts of the IP in the $(1+1)$ -dimensional Gross-Neveu (GN) model, but it can also exist without the presence of inhomogeneous condensates [33].

The model calculations with focus on IPs are predominantly restricted to the mean-field approximation, i.e., neglect bosonic quantum fluctuations. There is an ongoing discussion whether IPs persist when going beyond this approximation [34–39] or whether alternative scenarios such as liquid-crystal behavior [4, 5, 40, 41] or the so-called quantum pion liquid regime [42–46] are realized through disordering by fluctuations of different types of Goldstone bosons. Typically, phases with symmetry breaking such as the HBP and the IP are weakened by quantum and/or thermal fluctuations [5, 34, 36, 47, 48]. However, these findings are either based on low-dimensional model calculations or involve drastic approximations. Thus, clarifying the fate of the IP beyond the mean-field approximation in theories with more relevance for phenomenology is an important future direction in the investigation of the QCD phase diagram.

An obvious and necessary first step in this direction, is to study the regularization scheme (RS) and regulator dependence of the IP in mean-field theory before extending state of the art lattice field theory simulations of the IP in NJL-type models [34, 37, 49] to $(3+1)$ -dimensions. Recently, it has been demonstrated in the $(2+1)$ -dimensional GN model that the existence and shape of the IP strongly depends on the used RS and on the respective value of the regulator [50, 51]. Moreover, in this model and also other related four-fermion models in $2+1$ dimensions, the IP is only present at finite values of the regulator. The IP is absent in the renormalized limit [52]. This observation could be of particular relevance in the $(3+1)$ -dimensional NJL model, which is non-renormalizable. Its phase diagram obtained within different continuum RSs was compared in Ref. [53] with the main result that all three expected phases (SP, HBP, IP) are present in the phase diagram, but with large quantitative differences. This study, however, compared the RSs only at a single parameter set for each RS, where central observables such as the constituent quark mass in the vacuum did not agree between the RSs.

In the present work, we significantly extend and improve this study in several ways. First, we determine the phase diagrams within different RSs for a large range of constituent quark masses, which allows to compare in a more systematic and physically meaningful way. Second, we include three lattice discretizations as additional RSs in the comparison. This is particularly interesting, since lattice Monte-Carlo simulations would be an ideally suited approach to study the phase diagram of this model beyond the mean-field approximation in a rigorous way. Moreover, we investigate the effect of excluding the medium part of the theory (which are finite without regularization) from the regularization. This was already shown to have a strong effect on certain features of the NJL model and can, e.g., cure causality violations that

otherwise arise at finite density within cutoff schemes [54]. Finally, we add a completely new direction and investigate the existence, extent and RS dependence of the moat regime in the phase diagram at both zero and non-zero temperature and chemical potentials.

This paper is organized as follows. In Section II we recapitulate the definition of the NJL model and derive all relevant quantities for the study of its phase diagram. Furthermore, we briefly discuss the five employed RSs and the parameter matching, which is based on the quark constituent mass M_0 and the pion decay constant f_π . In Section III we present the results regarding the IPs including the phase diagram for each of the studied RSs in the (M_0, μ) -plane at zero temperature. Results for the moat regime for both $T = 0$ and $T \neq 0$ are discussed in Section IV. We conclude in Section V.

II. THE NAMBU-JONA-LASINIO MODEL IN $3+1$ DIMENSIONS

The action of the $(3+1)$ -dimensional NJL model in Euclidean spacetime is

$$S[\bar{\psi}, \psi] = \int_0^\beta d\tau \int d^3x \left\{ \bar{\psi} (\not{\partial} + \gamma_0 \mu) \psi + G \left[(\bar{\psi} \psi)^2 + (\bar{\psi} \gamma_5 \boldsymbol{\tau} \psi)^2 \right] \right\}, \quad (1)$$

where $\bar{\psi}$ and ψ are fermion fields, describing massless quarks, with $\bar{N} = N_f \times N_c \times N_\gamma = 2 \times 3 \times 4$ components (representing the number of quark flavors, colors and spin components, respectively). We use the slash notation $\not{\partial} = \gamma_\mu \partial_\mu$, where the matrices γ_μ fulfill the Clifford algebra for a Euclidean metric. The spacetime integration is restricted to $[0, \beta] \times \mathbb{R}^3$ with anti-periodic boundary conditions for the fermion fields in the imaginary time direction. The temporal extent β is given by the inverse temperature $1/T$, μ is the quark chemical potential and $\boldsymbol{\tau}$ is the vector of Pauli matrices acting in flavor space. The coupling constant G can be tuned such that certain vacuum observables agree with corresponding experimental values, e.g., the pion decay constant (see Section IID).

The action (1) is invariant under global $U(1) \times SU_V(2) \times SU_A(2)$ transformations with the generators $\mathbb{1}, \boldsymbol{\tau}, \boldsymbol{\tau} \gamma_5$, which is the chiral symmetry group in the massless limit of 2-flavor QCD.

To get rid of the four-fermion term, one typically introduces bosonic auxiliary fields σ and $\boldsymbol{\pi}$ via a Hubbard-Stratonovich transformation. The resulting partition function with action

$$S[\bar{\psi}, \psi, \sigma, \boldsymbol{\pi}] = \int d^4x \left\{ \bar{\psi} D \psi + \frac{\sigma^2 + \boldsymbol{\pi}^2}{4G} \right\}, \quad (2)$$

where

$$D = \not{\partial} + \gamma_0 \mu + \sigma + i \gamma_5 \boldsymbol{\tau} \cdot \boldsymbol{\pi}, \quad (3)$$

provides access to mesonic degrees of freedom in a more obvious way and is equivalent to the purely fermionic partition function. The expectation values of the bosonic fields satisfy the Ward identities

$$\langle \bar{\psi}\psi \rangle = -\frac{1}{2G} \langle \sigma \rangle, \quad \langle \bar{\psi}i\gamma_5\boldsymbol{\tau}\psi \rangle = -\frac{1}{2G} \langle \boldsymbol{\pi} \rangle, \quad (4)$$

and, thus, can be used as indicators for the spontaneous breaking of the chiral symmetry $SU_A(2)$. The symmetry transformations $SU_V(2) \times SU_A(2)$ on the level of the purely fermionic action (1) correspond to $O(4)$ rotations of the field vector $\phi = (\sigma, \boldsymbol{\pi})$ for the action (2).

As the fermion fields appear exclusively in a bilinear form in the action (2), the corresponding integration over Grassmann variables can be carried out, resulting in a purely bosonic path integral,

$$Z = \int \mathcal{D}\sigma \mathcal{D}\boldsymbol{\pi} e^{-S_{\text{eff}}[\sigma, \boldsymbol{\pi}]}, \quad (5)$$

with the effective action

$$S_{\text{eff}}[\sigma, \boldsymbol{\pi}] = \int_0^\beta d\tau \int d^3x \frac{\sigma^2 + \boldsymbol{\pi}^2}{4G} - \text{Tr} \ln D. \quad (6)$$

We restrict this work to the mean-field approximation, where fluctuations of σ and $\boldsymbol{\pi}$ are suppressed. On the one hand this is a severe simplification compared to the full quantum field theory. On the other hand the dependence on the fermionic ultra-violet (UV)-regularization is still present within this approximation. The mean-field approximation is often considered as an appropriate starting point that is computationally less expensive than fully non-perturbative calculations with functional methods or lattice simulations.

Within the mean-field approximation, the integration over σ and $\boldsymbol{\pi}$ in the partition function (5) is reduced to the contribution of a single field configuration, which is the global minimum of S_{eff} with respect to the bosonic fields, i.e., the functional integration in the partition function is reduced to a minimization problem. In case of a spontaneously broken symmetry, one finds multiple degenerate minima. In the mean-field approximation, however, it is appropriate to simply pick one of the equivalent minima, see, e.g., Refs. [19, 25, 55–57] for corresponding discussions.¹

In this work, we restrict the bosonic fields to exhibit only a spatial, but not a temporal dependence, i.e., $\phi(x) = \phi(\vec{x})$, where $\vec{x} = (x_1, x_2, x_3)$. A further simplifying restriction, which we impose for a few specific calculations, is the restriction to homogeneous bosonic field $\sigma, \boldsymbol{\pi} = \bar{\sigma}, \bar{\boldsymbol{\pi}}$. In this particular case, the $O(4)$ symmetry allows to set $\bar{\boldsymbol{\pi}} = 0$.

A. Homogeneous effective potential

Evaluating the $\ln \text{Det } D$ contribution in S_{eff} analytically is in general not possible for arbitrary field configurations. While some specific 1-dimensional modulations of the bosonic fields admit an expression of $\ln \text{Det } D$ by knowledge of the density of states [23, 58–60], one knows the exact eigenvalues for homogeneous bosonic fields, as they coincide with eigenvalues of free fermions with the dynamically generated fermion mass $m = M = \sqrt{\bar{\sigma}^2 + \bar{\boldsymbol{\pi}}^2}$. The homogeneous, effective potential is defined as

$$U(M, \mu, T) = \frac{1}{\beta V} S_{\text{eff}}[\bar{\sigma}, \bar{\boldsymbol{\pi}}] \quad (7)$$

and can be rewritten into a compact form containing a simple momentum integral

$$U(M, \mu, T) = \frac{M^2}{4G} - \frac{\bar{N}}{2} l_0(M, \mu, T), \quad (8)$$

(see, e.g., Refs. [61, 62]). Here, V is the spatial volume, for which we typically consider the limit $V \rightarrow \infty$ and l_0 is a UV-divergent momentum integral that is defined in Eq. (B1).

If the ground state of the system, at given μ and T , is given by a homogeneous condensate, the homogeneous effective potential evaluated at its global minimum $M = \bar{\Sigma}$ is equal to the thermodynamic grand potential, i.e., $\Omega(\mu, T) = U(\bar{\Sigma}, \mu, T)$. The configuration $\bar{\Sigma}(\mu, T)$ can be determined using the gap equation

$$\left. \frac{\partial U}{\partial M} \right|_{M=\bar{\Sigma}} = 0 \Rightarrow M \left(\frac{1}{2G} - N l_1(M, \mu, T) \right) \Big|_{M=\bar{\Sigma}} = 0, \quad (9)$$

where l_1 is a UV-divergent integral, which requires regularization, and is defined in Eq. (C2). If there is more than one solution of Eq. (9), one can determine the global minimum by inserting each of them in Eq. (8) and comparing the corresponding values of U .

The appearing divergences in U and l_1 are dependent on M and cannot be compensated by G . Thus, the regulator cannot be removed using a renormalization prescription as in renormalizable quantum field theories. The results will instead depend on both the chosen RS and the respective regulator Λ . In other words, the RS becomes to some extent part of the theory and Λ can be understood as a parameter of the theory. We discuss more about the role of Λ in Section IID. More detailed formulas for U and l_1 can be found in Appendix B and Appendix C, respectively.

B. Stability analysis

There are two common approaches to investigate inhomogeneous condensates. Either one minimizes the ef-

¹ In case of a first order phase transition, one finds multiple degenerate minima, which are not connected by symmetry transformations. In this case we refrain from evaluating observables directly at the phase boundary line in order to avoid ambiguities.

fective action in the space of inhomogeneous field configurations to find the energetically favored solution or one tests the stability of homogeneous configurations against inhomogeneous perturbations. While the minimization strategy obviously provides the full information about the thermodynamic ground states, it either requires a parametrization of the inhomogeneous condensate or one minimizes the condensate in a lattice discretized theory, which demands expensive numerical computations including continuum and infinite volume limit. Especially in higher-dimensional models there are open questions about the preferred form and dimensionality of the inhomogeneous modulation. The stability analysis method on the other hand requires no ansatz and is comparatively cheap and flexible, meaning that it can be used in a straightforward way with various regularization schemes. However, it comes with the disadvantage that it does not give conclusive information about the preferred shape of the inhomogeneous condensate. Moreover, the existence of an instability of $\bar{\Sigma}$ towards an inhomogeneous perturbation is a sufficient, but not necessary condition for the existence of an IP.

Stability analyses are our main tool to explore the existence and properties of IPs in the present work. This approach has been used extensively in investigations of the NJL model as well as other four-fermion and Yukawa models within various RSs, e.g. in Refs. [22, 33, 50, 52, 63–72]. Therefore, we only recapitulate the core idea and refer to Ref. [67] for a discussion and derivation in the context of the NJL model, to Ref. [50] for a discussion of stability analysis in combination with a lattice regularization and to Ref. [33] for a detailed investigation of the range of validity of this method. The starting point of a stability analysis is to consider an infinitesimal inhomogeneous perturbation of arbitrary form $\delta\phi(\vec{x})$ of a homogeneous field configuration $\bar{\sigma}$. One then expands the effective action in powers of this perturbation, where the first order correction is proportional to the left-hand side of the gap equation (9), which vanishes, if one considers a minimum of the homogeneous effective potential, i.e., $\bar{\sigma} = 0$ or $\bar{\sigma} = \bar{\Sigma}$, as an expansion point. The coefficients of the second order correction correspond to the curvature of the effective action in the direction of the respective inhomogeneous perturbation. For a perturbation of momentum \mathbf{q} to the bosonic field ϕ , where ϕ is either σ or π_i , this is given by the bosonic 1-particle irreducible two-point vertex function $\Gamma_\phi^{(2)}(\mathbf{q})$, for simplicity denoted as bosonic two-point function in the following.² If one finds negative values of $\Gamma_\phi^{(2)}(\mathbf{q})$ for any ϕ and $\mathbf{q} \neq 0$, there exists an inhomogeneous field configuration, which is energetically favored over the homogeneous expansion point. If this expansion point is the global homogeneous minimum $\bar{\Sigma}$, a negative value of $\Gamma^{(2)}$ signals

that the corresponding inhomogeneous configuration is favored over any homogeneous configuration. To summarize, the check for an IP at given (μ, T) , requires two steps, (1) the determination of $\bar{\Sigma}(\mu, T)$ and (2) the computation of $\Gamma_\phi^{(2)}(\mathbf{q})$, where negative values indicate the presence of an IP.

For the Pauli-Villars (PV) and spatial momentum cutoff (SC) schemes, $\Gamma_\phi^{(2)}(\mathbf{q})$ can be split up into two divergent contributions stemming from the fermionic loop integral: l_1 , which does not depend on \mathbf{q} and also appears in the gap equation (9), and $l_2(\mathbf{q})$, see Eq. (C1). For the lattice discretizations, this is not possible and the remaining loop integral $l_{3,\phi_i}(\mathbf{q})$ depends on the chosen lattice discretization, compare Eq. (C28) and Eq. (C29) respectively. Further details on the evaluation of $\Gamma_\phi^{(2)}(\mathbf{q})$ can be found in Appendix C and on the regularization schemes in Section II C.

Moat regime

A moat regime is characterized by a non-trivial bosonic dispersion relation with a global minimum at a non-zero momentum. In contrast to an IP, the two-point function, which allows to read off the dispersion relation, does not have to exhibit a negative value at this minimum. A simple criterion characterizing a moat regime is a negative sign of the wave-function renormalization $Z_\phi = z_\phi(M = \bar{\Sigma})$, ($\phi = \sigma, \pi_i$) [33], where

$$z_\phi(M) = \left. \frac{d\Gamma_\phi^{(2)}(q)}{dq^2} \right|_{q=0}. \quad (10)$$

This criterion might fail to detect a moat regime, when the non-trivial, global minimum in $\Gamma^{(2)}$ is related to a higher-order derivative of the two-point function, i.e. when $\Gamma^{(2)}$ has a local minimum at $q = 0$ instead of a local maximum. We are, however, not aware of any work observing such a scenario in a renormalizable model.³

The formulas obtained for $z_\phi(\bar{\sigma}, 0)$ in the considered RSs can be found in Appendix D.

C. Regularization schemes

Both the calculation of the homogeneous effective potential and the stability analysis involve the evaluation of fermionic loop integrals that are UV-divergent. In this work, we use and compare several schemes and we discuss in the following how the schemes regulate such integrals.

² We note that the bosonic two-point function is by derivation diagonal in momentum space for theories with local four-fermion (FF) interaction channels, see, e.g., Refs. [33, 50, 52].

³ Later, we will discuss a case in the NJL model (which is non-renormalizable), where the two-point function shows exactly this behavior. It is, however, in a parameter region clearly outside the range of validity of the model.

We consider the generic integral

$$I = \frac{1}{\beta} \sum_{n=-\infty}^{\infty} \int \frac{d^3 p}{(2\pi)^3} f(\nu_n, \mathbf{p}, M), \quad (11)$$

where \mathbf{p} are spatial loop momenta, ν_n are the fermionic Matsubara frequencies and f is the integrand, which is a combination of free fermion propagators with mass M . This integral is UV-divergent when $f \propto p^a$ with $a \geq -3$ for large p . This is the case for the integrals l_1 and l_2 (for the SC and PV scheme) as well as l_{3,ϕ_i} (for the lattice discretizations).

1. Pauli-Villars

The PV regularization scheme introduces additional copies of the integrand with differing coefficients and masses. These can be interpreted as contributions from both bosonic and fermionic replica fields of the original fermionic fields. The integral (11) is then of the form

$$I^{(\text{PV})} = \frac{1}{\beta} \sum_{n=-\infty}^{\infty} \int \frac{d^3 p}{(2\pi)^3} \sum_{k=0}^{N_{\text{PV}}} c_k f(\nu_n, \mathbf{p}, M_k), \quad (12)$$

where $M_k = \sqrt{M^2 + \alpha_k \Lambda}$ and the $k = 0$ term with $\alpha_0 = 0$ is the unregularized contribution. The number of regulating terms N_{PV} is not fixed and only bounded from below. For our investigation of the (3 + 1)-dimensional NJL model, $N_{\text{PV}} \geq 2$ is necessary to render the most divergent integral finite. The coefficients c_k and α_k need to fulfill the conditions

$$\sum_{k=0}^{N_{\text{PV}}} c_k = 0, \quad \sum_{k=0}^{N_{\text{PV}}} c_k \alpha_k = 0, \quad (13)$$

see, e.g., Refs. [56, 73]. We follow existing literature and choose $N_{\text{PV}} = 3$, $\vec{c} = (1, -3, 3, -1)$ and $\vec{\alpha} = (0, 1, 2, 3)$ [23].

2. Spatial momentum cutoff

With the SC scheme one restricts the region of integration of the spatial loop momenta to a 3-dimensional sphere of radius Λ . The integral (11) is then replaced by

$$I^{(\text{SC})} = \frac{1}{\beta} \sum_{n=-\infty}^{\infty} \int \frac{d\Omega}{(2\pi)^3} \int_0^\Lambda dp p^2 f(\nu_n, \mathbf{p}, M), \quad (14)$$

where $\int d\Omega$ represents the angular integration over the loop momenta. One of the main drawbacks of this scheme is that shifts of the integration variable p lead to a modification of the integration boundaries, which can severely complicate the evaluation of such integrals.⁴

⁴ A possible variation of such cutoff schemes is to introduce an energy cutoff instead of a momentum cutoff as proposed, e.g., in Refs. [74, 75].

3. Lattice regularizations

Lattice regularizations lead to momentum integrals similar to those in the SC scheme. For infinite space-time volume⁵ Eq. (11) becomes

$$I^{(\text{Lattice})} = \prod_{i=0}^3 \left[\int_{-\Lambda_{\text{LFT}}}^{\Lambda_{\text{LFT}}} dp_i \right] f'(p_0, \mathbf{p}, M), \quad (15)$$

where $\Lambda_{\text{LFT}} = \pi/a$ with lattice spacing a and a modified integrand, f' containing free fermion propagators for the respective lattice fermion discretization as discussed in the following paragraphs.

a. SLAC fermions In the SLAC discretization [76, 77] the derivative operator is constructed such that the dispersion relation of a massless fermion matches the linear continuum dispersion relation of a massless fermion within the first Brillouin zone.⁶ As a consequence, one finds that this discretization fully respects chiral symmetry and is free of doublers. This construction, however, necessitates a discontinuity of the dispersion relation at the edge of the Brillouin zone. While this causes severe problems in gauge theories [78], the SLAC discretization has been successfully applied in the investigation of FF models [34, 35, 37, 79, 80].

Within this discretization, one finds for the fermion propagator

$$S_{\text{SLAC}}(p) = \frac{-i\gamma_\mu \mathcal{P}_{\text{SLAC}}(p_\mu) - \gamma_0 \mu + M}{\sum_{i=0}^3 (\mathcal{P}_{\text{SLAC}}(p_i) - \delta_{i,0} i\mu)^2 + M^2} \quad (16)$$

with dispersion relation

$$\mathcal{P}_{\text{SLAC}}(p_\mu) = 2\Lambda_{\text{LFT}} \left(\frac{p_\mu}{2\Lambda_{\text{LFT}}} - \left\lfloor \frac{1}{2} + \frac{p_\mu}{2\Lambda_{\text{LFT}}} \right\rfloor \right), \quad (17)$$

where $\lfloor \cdot \rfloor$ denotes the floor function.

b. Hybrid fermions This discretization is a combination of the SLAC discretization for the temporal derivative in the action and a naive lattice discretization for the spatial derivatives. The naive discretization also respects chiral symmetry, but exhibits 2^d fermion doublers, where $d = 3$ is the number of naively discretized dimensions. It gives rise to a sinusoidal dispersion relation and one finds for the fermion propagator

$$S_{\text{Hybrid}}(p) = \frac{-i\gamma_0 [\mathcal{P}_{\text{SLAC}}(p_0) - i\mu] - i \sum_{i=1}^3 \gamma_i \sin(\mathbf{a}\mathbf{p}_i) + M}{(\mathcal{P}_{\text{SLAC}}(p_0) - i\mu)^2 + \sum_{i=1}^3 \sin^2(\mathbf{a}\mathbf{p}_i) + M^2}. \quad (18)$$

⁵ For finite spacetime volume, one finds that integrals over momenta in directions with a finite extent are replaced by sums. However, since we consider lattice regularizations almost exclusively in an infinite spacetime volume, i.e., $T = 0$ and $1/V = 0$, we abstain from giving the respective formulas.

⁶ This discretization is sometimes also called the plane wave expansion.

The existence of fermion doublers in this discretization necessitates additional modifications of the action. Without such modifications, one finds that at large momenta the bosonic fields mediate unphysical interactions between different doubler species in the Yukawa-interaction terms [82]. One can suppress these unwanted interactions by introducing in momentum space a weight function \tilde{W} to the Yukawa-interaction terms

$$\begin{aligned} & \tilde{\psi}(p) (\tilde{\sigma}(p-q) + i\gamma_5 \boldsymbol{\tau} \tilde{\boldsymbol{\pi}}(p-q)) \tilde{\psi}(q) \\ & \rightarrow \tilde{\psi}(p) \tilde{W}_X(\mathbf{p}-\mathbf{q}) (\tilde{\sigma}(p-q) + i\gamma_5 \boldsymbol{\tau} \tilde{\boldsymbol{\pi}}(p-q)) \tilde{\psi}(q), \end{aligned} \quad (19)$$

where $\tilde{\psi}, \tilde{\sigma}, \tilde{\boldsymbol{\pi}}$ are the Fourier components of the respective fields and $\tilde{W}_X(\mathbf{p}-\mathbf{q}) = \prod_{i=1}^3 \tilde{w}_X(p_i - q_i)$. There are infinitely many possible choices for \tilde{w}_X , which lead to a suppression of the interactions between the doublers and to identical results for renormalizable theories in the continuum limit. We consider the two possibilities

$$\tilde{w}_{\cos}(p_\mu) = \frac{1 + \cos(p_\mu)}{2} \quad (20)$$

and

$$\tilde{w}_{\Theta}(p_\mu) = \Theta(1 - |p_\mu| \frac{2a}{\pi}). \quad (21)$$

Since the 3+1-dimensional NJL model is a theory, where one cannot take the continuum limit, these two choices are not equivalent, and we thus consider them as separate RSs denoted as Hybrid_{cos} and as Hybrid_Θ, respectively.

4. No medium regularization

Within some RSs one can separate the integral I into a medium part dependent on μ and T and a vacuum contribution independent of such thermodynamical quantities. In this work, this is the case for the PV scheme and SC scheme. In our context, only the vacuum contributions are UV-divergent while medium contributions stay finite, since the respective integrand vanishes at large momenta due to exponential suppression by the Fermi-Dirac distribution functions. After regularization and for chemical potentials and/or temperatures that are in the order of or larger than the regulator, one finds that the fall-off of the integrand in the medium contribution is modified, e.g., cut off in the case of the SC scheme. In a renormalizable theory, where the regulator is removed at the end, it does not make a difference, whether the whole theory or only the vacuum parts are regulated. However, as we need to keep the regulator finite it might be advantageous to reduce the regularization artifacts by only regulating the UV-divergent parts. We indicate such a version of a RS, that allows the separation of vacuum and medium parts, as no medium regularization (NMR).

Applying NMR was found to have a significant positive impact on the homogeneous phase diagram [83] and physical quantities such as the speed of sound, which can

violate causality in a large region of the phase diagram for the SC without NMR [54].

In our case, NMR is equivalent to renormalization group consistency, which is discussed in Ref. [84] and provides a systematic approach to correct for regularization artifacts in the medium contributions without explicitly separating them from the vacuum parts.

D. Parameter tuning

As discussed in Section II A, we need to consider the regulator Λ as a parameter of the theory, in addition to the coupling G . When interpreting the NJL model as a low-energy model for chiral symmetry breaking in QCD, the value of Λ represents the energy scale, where the gluon dynamics start to become dominant and the approximation of the gluon-mediated interactions as FF vertices is no longer valid [73].

The coupling G and the regulator Λ can be tuned such that certain standard observables assume physically motivated values. We follow an approach proposed in Ref. [73], which has become a standard in NJL model investigations (see, e.g., Refs. [19, 25, 54, 67, 81]), namely to fix the pion decay constant $f_\pi = 88 \text{ MeV}$.⁷ The constituent quark mass in the vacuum $M_0 = \bar{\Sigma}(\mu = 0, T = 0)$ is the second key quantity that is used as input in the tuning. To relate f_π and M_0 to G and Λ , we follow Ref. [73] and present corresponding formulas for G and f_π/M_0 in Appendix A.

III. REGULARIZATION SCHEME DEPENDENCE OF THE INHOMOGENEOUS PHASE AT ZERO TEMPERATURE

A. General phase structure

We start the discussion by considering the central result of this work: the phase structure within different RSs in the (M_0, μ) -plane at $T = 0$ as shown in Fig. 1. From this figure it is obvious that there is a strong dependence of both the existence and the extent of IPs on the RS and the regulator Λ . This ambiguity indicates that predictions of an IP in the NJL model have rather limited implications for the phase structure of QCD.

In Fig. 1, moving along the horizontal axis corresponds to considering different values for M_0 , i.e., different parameter sets with f_π being fixed. It is noteworthy that the value of f_π only sets the scale in MeV in the plots and does not change the phase structure, see Section II D. In the plot, the HBP is located at small chemical potential,

⁷ In QCD with physical quark masses, one would expect $f_\pi \approx 92.4 \text{ MeV}$ [85]. However, using chiral perturbation theory one finds for vanishing bare quark masses $f_\pi \approx 88 \text{ MeV}$ [86, 87].

i.e., below the phase boundary lines. While the homogeneous phase boundaries (solid and dotted lines) are qualitatively similar between the RSs, we find that the shape and extent of the IP (shaded regions) in this plane is highly dependent on the choice of the RS. In particular, we note that there is not a single point in the (M_0, μ) -plane, where all RSs exhibit an IP simultaneously. For small values of M_0 , which correspond to large values of Λ , we find that the IP is absent within all RSs, which is the only region where the RSs agree with respect to the existence of the IP.

We note that the observed strong dependence of the existence and extent of the IP in the NJL model on the RS and the value of the regulator is not surprising: IPs appear for values of the chemical potential, which are of the order of the regulator, which facilitates strong regularization artifacts.

In the following we briefly discuss the results obtained within each of the RSs:

- The PV scheme leads to the largest IP in the (M_0, μ) -plane. One finds that the CP and the LP coincide in agreement with previous studies [23, 24]. For intermediate values of $M_0 < 315\text{MeV}$, one finds two separated regions: the “inhomogeneous island”, which is connected to the HBP and the “inhomogeneous continent” [88], which is located at larger values of μ and disconnected from the HBP. For small values of M_0 , the “inhomogeneous island” is absent and only the “inhomogeneous continent” is present.
- Within the SC scheme the IP in the (M_0, μ) -plane is significantly smaller compared to that of the PV scheme. One finds that the CP and the LP are separated, which is due to surface terms that arise in the underlying loop integrals [24].
- Within the SLAC discretization one finds that an “inhomogeneous continent” splits off at an intermediate value of M_0 similar as in the PV scheme. Moreover, a splitting of the CP and the LP is observed similar to the findings within the SC scheme. The extent of the IP, however, is larger than that of the SC scheme. The depicted phase boundaries exhibit small but clearly visible statistical fluctuations, which are a consequence of the stochastic evaluation of the underlying momentum integrals.
- Within the Hybrid $_{\Theta}$ scheme, an IP is present for small values of M_0 and μ . The CP and LP are separated, but the splitting is in the opposite direction compared to the SC and SLAC scheme, i.e., the LP is located at larger values of M_0 than the CP. This is mostly likely due to the effective vector interactions that arise as discretization artifacts in Yukawa-theories with schemes that exhibit fermion doublers such as the Hybrid schemes [34, 82]. Such vector actions are known to split the CP and the

LP in the NJL model such that the LP is located at a higher temperature [89, 90].

- It is particularly important to note that no instability region is observed at all in the Hybrid $_{\text{cos}}$ scheme. Since the homogeneous phase boundary line is by definition identical to the one of the Hybrid $_{\Theta}$ scheme, we abstain from plotting it separately.

In the following sections, we will elaborate more on the significant, qualitative differences in the results obtained within different RSs.

A related finding with respect to the RS scheme dependence of the IPs is the study of the phase diagram of the $d + 1$ -dimensional GN model in Refs. [63, 64, 91], where an IP is present for $d \in [1, 2)$ and absent for $d \in [2, 3)$. The GN model is also non-renormalizable for $d = 3$ and the results from Refs. [63, 64] can be interpreted as a study of the $3 + 1$ -dimensional GN model using dimensional regularization. A small d would then correspond to a strongly-regularized theory, i.e., a small value of Λ within RSs considered in this work. The integral expression for the bosonic two-point function of the σ field is mathematically identical in the GN model and the NJL model (independent of $d = 1, 2, 3$) and the IP in the NJL model typically is realized through inhomogeneities in the σ condensate [23]. Thus, these studies provide results within a sixth RS scheme pointing towards the non-existence of an IP for higher values of Λ (high values of d in dimensional regularization), consistent with the other five RSs.

B. Two-point functions

In this section, we study the rather different behavior of the two-point functions within all five RSs to illustrate possible reasons for the vastly different phase diagrams discussed in the previous section and shown in Fig. 1. Fig. 2 depicts the bosonic two-point function $\Gamma_{\sigma}^{(2)}$ as a function of the bosonic momentum q for all considered RSs and selected values of the chemical potential μ , $T = 0$, $M_0 = 300\text{MeV}$.

One finds that the PV and SC scheme exhibit a crudely similar behavior of the two-point function. There are, however, visible differences in terms of a vertical shift as well as of the depth of the minima, which cause the absence of an instability for the SC scheme, while it is present in the PV scheme (see the left plot).

The lattice discretizations exhibit a periodic two-point function, which is a consequence of the periodic dispersion relations on the lattice. The SLAC discretization exhibits a non-zero positive slope at $q = 0$ for all μ , which is a consequence of the jump in the fermionic dispersion relation at the edge of the Brillouin zone. This can lead to a maximum in the two-point function at a finite momentum, while a minimum can be present for

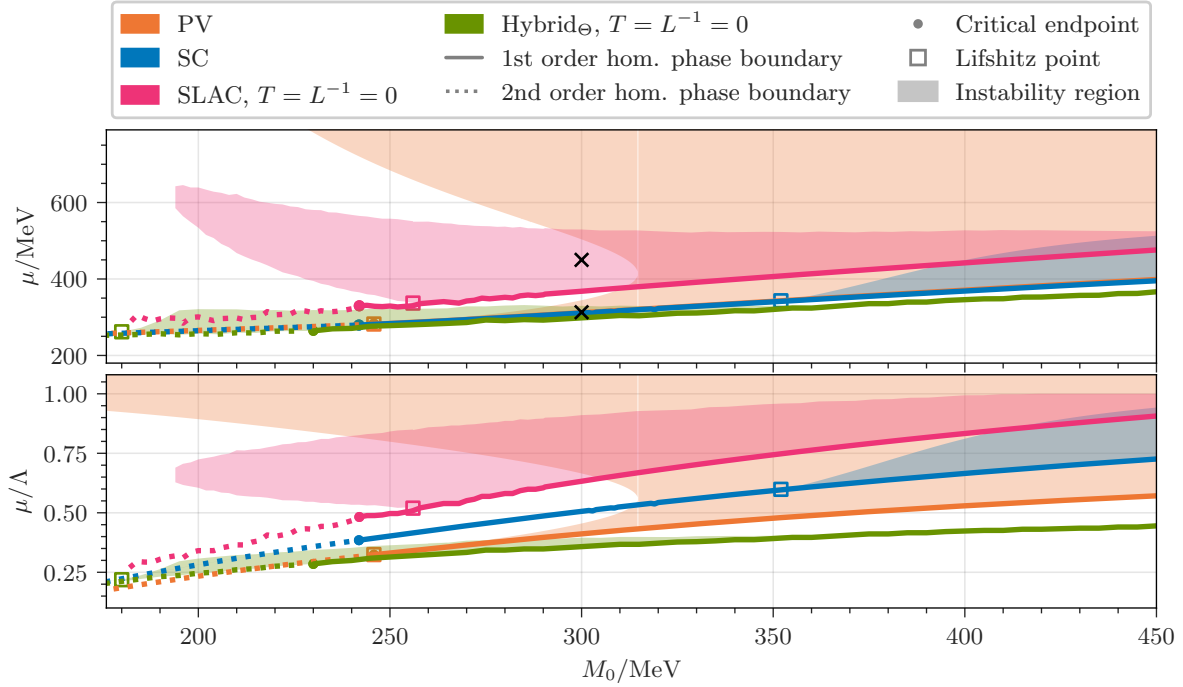


FIG. 1. The homogeneous phase diagram and the regions of instability towards an IP in the (M_0, μ) -plane at $T = 0$ within four RSs. Both plots depict the same data, where the upper plot the chemical potential is given in units of MeV, while the lower plot gives μ in units of the respective Λ , which is a function of M_0 . The solid and dotted lines represent first and second order homogeneous phase boundaries respectively obtained by a minimization of the effective potential. The circle represents the CP that separates these boundaries. The shaded regions are the instability regions where the bosonic two-point function exhibits negative values for non-zero spatial momenta. The open squares indicate the position of the LP. The black crosses mark (M_0, μ) values chosen for the plots in Fig. 2. The data for the Hybrid $_{\cos}$ scheme is not shown as it does not exhibit any instability region and the homogeneous phase boundary is identical to that obtained in the Hybrid $_{\Theta}$ scheme.

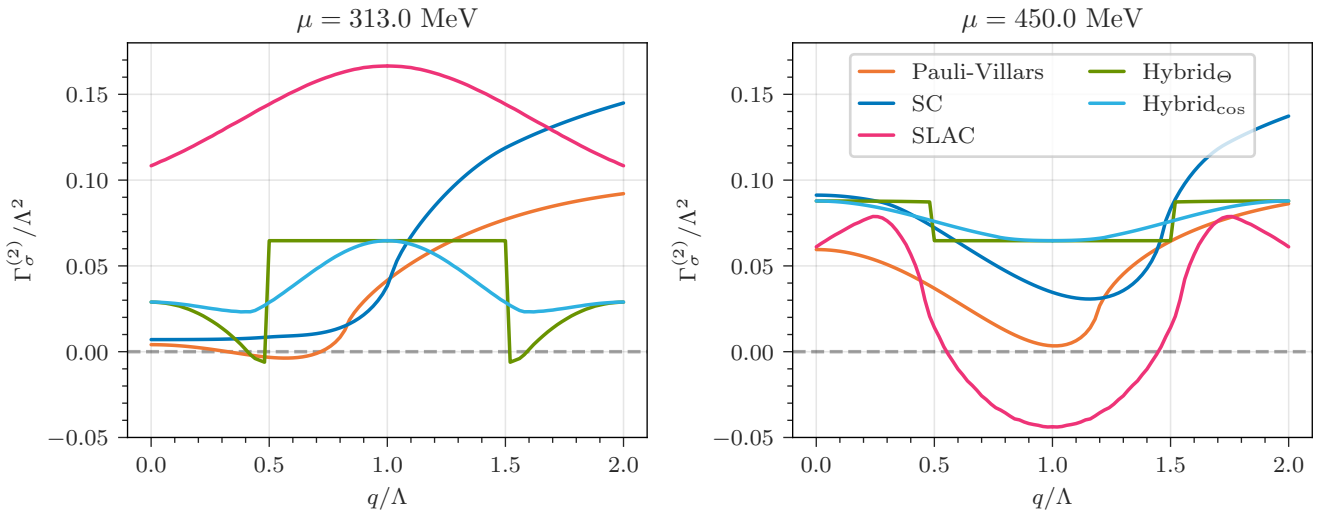


FIG. 2. The bosonic two-point function $\Gamma_{\sigma}^{(2)}$ as a function of the bosonic momentum q for chemical potential $\mu = 313$ MeV, 450 MeV at $T = 0$ and $M_0 = 300$ MeV. Different colors represent different RSs. The black crosses in Fig. 1 mark points in the (M_0, μ) -plane these plots correspond to.

even larger momenta, as is the case in the right plot of Fig. 2.

The Hybrid discretizations exhibit rather different two-point functions because of differences in the respective weighting functions. This is especially evident with the Hybrid_Θ scheme, where the two-point function jumps at $q = \Lambda_{\text{LFT}}/2$ to large positive values due to the discontinuous weighting function (cf. Eq. (21)). At the chosen chemical potential in the left plot of Fig. 2, the two-point function is negative for small momenta signaling an instability towards an IP. For increasing μ these negative intervals are shifted towards larger q and finally disappear, because they are suppressed by the weighting function. In contrast, the smooth weighting function in the Hybrid_{cos} scheme (cf. Eq. (20)) suppresses the two-point function already for small momenta causing the absence of instabilities which are present in the Hybrid_Θ scheme.

C. Characteristic momentum

The characteristic momentum Q is defined as that momentum, where the bosonic two-point function $\Gamma_{\sigma}^{(2)}(q)$ assumes its minimal value,

$$Q = \arg \min_q \Gamma_{\sigma}^{(2)}(q). \quad (22)$$

Even though this is not necessarily the dominating momentum of the inhomogeneous field configuration, which can, in principle, be obtained by minimizing S_{eff} , it is expected to be similar and, thus, a useful quantity to characterize an IP. On a second-order phase boundary between an SP and an IP, Q corresponds to the momentum of the inhomogeneous condensate [33]. By considering energy gaps at the Fermi surface and following the argumentation of the Peierls stability, one expects that $Q \approx 2\mu$ (see, e.g., Refs. [3, 25] for a discussion in the context of these models). However, the exemplary two-point functions discussed in Section III B have shown that this is in general not the case for the lattice regularization schemes.

To investigate the behavior of the characteristic momentum systematically, we define

$$Q'(\mu, T) = \begin{cases} Q(\mu, T) & \text{if } \Gamma^{(2)}(Q) < 0 \\ 0 & \text{otherwise} \end{cases}, \quad (23)$$

because only a characteristic momentum associated to an instability is relevant for this discussion. In Fig. 3, $Q'(\mu, T)$ is shown within different RSs in the (M_0, μ) -plane at $T = 0$. Within the PV and SC schemes one finds that the characteristic momentum indeed follows the expectation of $Q \approx 2\mu$. While this is the expected behavior, it is important to note that consequently $Q \gtrsim \Lambda$ within most parts of the instability region. This is highly problematic, since it prevents separation of scales in the system and the regulator Λ does not serve as the largest energy scale in the system anymore. In contrast, within

the SLAC discretization one finds that the characteristic momentum is constant, $Q = \Lambda_{\text{LFT}}$ within the instability region (Λ_{LFT} is the maximal momentum that is available on the lattice, as defined in Section II C 3). With the Hybrid_Θ scheme, one finds that the characteristic momentum is almost constant $Q = \Lambda_{\text{LFT}}/2$ within the instability region. This corresponds to the threshold, when the weighting function sets in. Note that in the two latter cases Q is not related to the chemical potential μ , as expected according to the discussion above, but to the momentum cutoff $\Lambda_{\text{LFT}} \propto 1/a$. A corresponding IP is then clearly an artifact of the regularization.

1. Dominating versus characteristic momentum within the SLAC discretization

As previously discussed, the characteristic momentum Q might not be identical to the dominating momentum of the corresponding inhomogeneous field configuration. We, therefore, investigate such field configurations for the SLAC discretization to check whether the inhomogeneous condensate actually oscillates with $Q = \Lambda_{\text{LFT}}$. To this end, we consider the SLAC discretized action in a finite spacetime volume $T^{-1} \times L^3 = 7.7 \times (7.4)^3 \text{ MeV}^{-4} = 30 \times 29^3 a^4$. Then, we perform minimizations of the effective action with respect to the bosonic fields. We restrict the minimization to 1-dimensional field configurations, to limit the numerical effort. This assumption is based on previous findings [92] where 1-dimensional field configurations were mostly favored. No further assumptions about the field configurations are made.

In a first step, we check and confirm that the two-point functions $\Gamma_{\sigma}^{(2)}(q)$ in the infinite spacetime volume and in the finite spacetime volume exhibit a similar behavior for $M_0 = 287 \text{ MeV}$ and $\mu = 380 \text{ MeV}$ (see Fig. 4). The upper plot in Fig. 5 then depicts the energetically preferred field configuration which was determined via the aforementioned minimization. We find $\pi(x) = 0$, which is in agreement with other continuum findings [56], while the σ field oscillates with the largest possible momentum, which is in agreement with the expectation from the characteristic momentum. This is also shown by the momentum distribution in the lower plot in Fig. 5. This confirms that the IP within the SLAC discretization indeed prefers a condensate which oscillates with the maximally possible momentum $\Lambda_{\text{LFT}} = \pi/a$. As discussed above, this is clearly an artificial behavior related to the RS but not a physically meaningful IP.

D. No medium regularization

In the above sections, we presented evidence and argued that strong regularization artifacts are present for $\mu/\Lambda \gtrsim 1$, which is the relevant region for IPs in the NJL model. As discussed in Section II C 4, NMR is a procedure to remove regularization artifacts in the medium

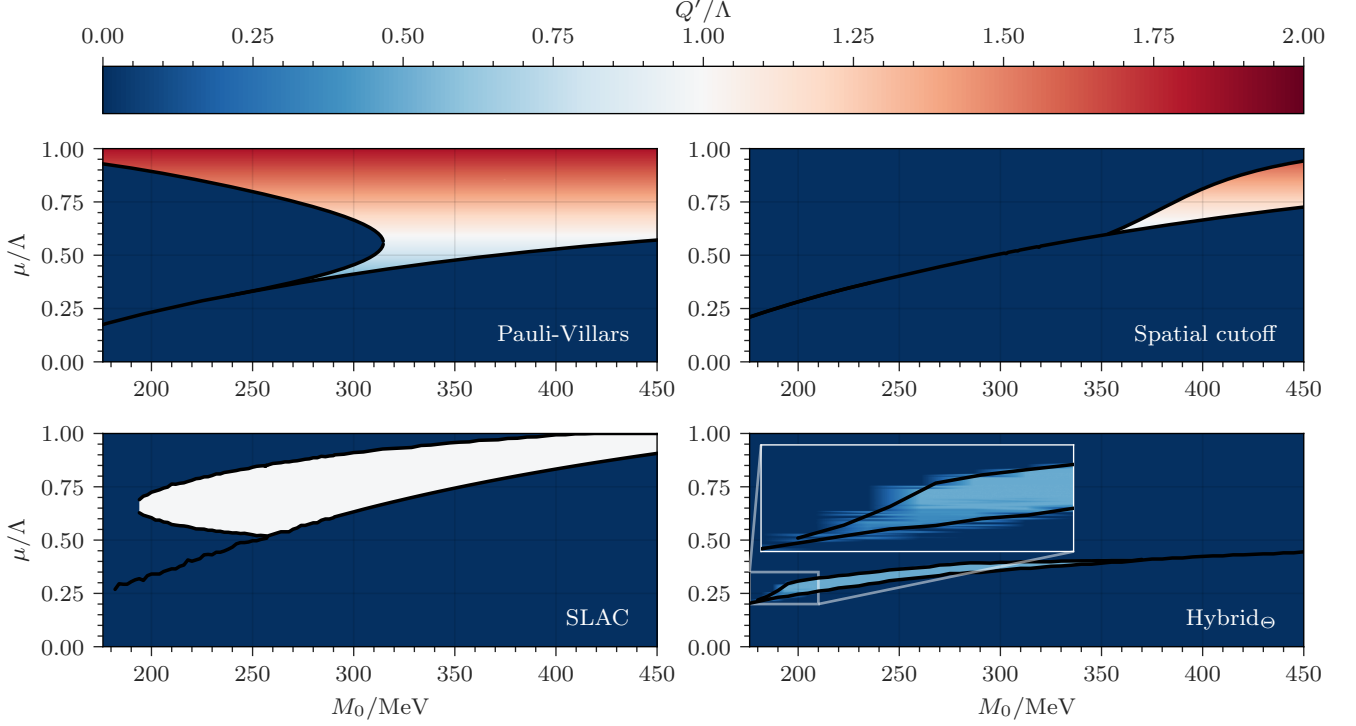


FIG. 3. The characteristic momentum $Q'(\mu, T)$ in the (M_0, μ) -plane at $T = 0$ within four RSs.

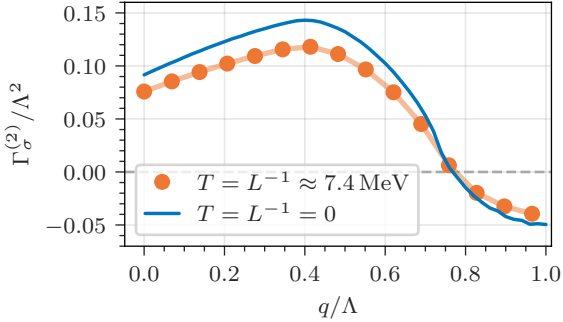


FIG. 4. The bosonic two-point function $\Gamma_\sigma^{(2)}$ as a function of the bosonic momentum q for the SLAC discretization in infinite $L^{-1} = T = 0$ and finite spacetime volume $T^{-1} \times L^3 = 7.7 \times (7.4)^3 \text{ MeV}^{-4} = 30 \times 29^3 a^4$ at $M_0 = 287 \text{ MeV}$ and $\mu = 380 \text{ MeV}$.

contributions of a given RS. Thus, it is expected that this procedure reduces the observed discrepancies between the different RSs. This is studied in the following within the SC and PV schemes.

Fig. 6 depicts the bosonic two-point function $\Gamma_\sigma^{(2)}$ as a function of the bosonic momentum q for three values of the chemical potential μ at $T = 0$ with the PV and the SC scheme with and without NMR. One finds that the NMR

has no impact on the results with the PV scheme for $\mu < \Lambda_{\text{PV}}$ (Λ_{PV} corresponds to the smallest mass of the regulating terms), which is a manifestation of the silver blaze phenomenon [93]. Similarly, the results of the SC scheme change marginally for small values of μ , but the impact of NMR becomes more significant for larger values of μ . At such values for μ , we observe for both schemes an unexpected behavior of the two-point function for small momenta without NMR, which is distinctly different from two-point functions in the instability regions as found in renormalizable 1+1-dimensional models [33, 69]. As visible in the right plot of Fig. 6, the SC scheme leads to a constant two-point function in an interval of small q , while within the PV scheme one finds a positive curvature of the two-point function at $q = 0$. However, both schemes exhibit a minimum of the two-point function for large momenta. We interpret this as artifacts stemming from the RSs. These artifacts are removed when using the NMR. The two-point functions then exhibit a qualitatively similar behavior for both schemes consistent with expectations from renormalizable 1+1-dimensional models.

Fig. 7 depicts the effect of NMR on the IP in the (M_0, μ) -plane at $T = 0$ for the PV and the SC scheme. The IP is unaffected for the PV scheme in the depicted region due to the mentioned silver-blaze like behavior and, thus, we only plotted the results without NMR. For the SC scheme, one finds that the IP has a different shape

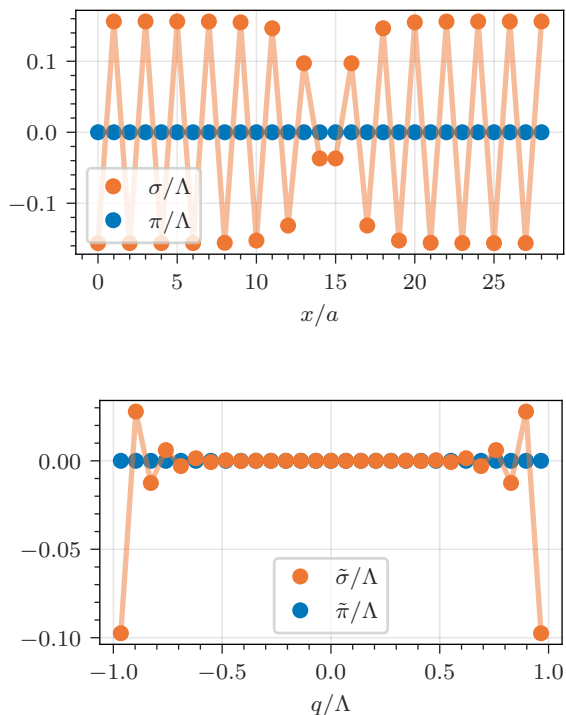


FIG. 5. The energetically preferred bosonic field configuration in position (**top**) and momentum space (**bottom**) for the SLAC discretization in finite spacetime volume $T^{-1} \times L^3 = 7.7 \times (7.4)^3 \text{ MeV}^{-4} = 30 \times 29^3 a^4$ at $M_0 = 287 \text{ MeV}$ and $\mu = 380 \text{ MeV}$.

and a significantly larger extent. Interestingly, there is a region where the SC scheme without NMR exhibits an instability region, while the SC scheme with NMR does not. We recognize that the shape of the IP in the SC scheme with NMR looks qualitatively similar to the shape of the IP in the PV scheme without NMR besides a global shift in M_0 . The residual differences are caused by differences in the vacuum parts of the relevant quantities, where NMR has no effect. Overall, our results suggest that the NMR procedure effectively reduces RS artifacts in the two-point functions, which leads to more consistent IPs between the PV and the SC schemes. However, even when using NMR, it is still unclear whether the NJL model has any predictive power for values of μ of the order or larger than the cutoff, where an IP can be observed.

IV. REGULARIZATION SCHEME (IN)DEPENDENCE OF THE MOAT REGIME

Following our analysis of the IP, we turn to the study of the moat regime. We focus on the PV and the SC schemes as these schemes give better insight into the analytic structure of the central quantities to understand this phenomenon. Both schemes exhibit significantly dif-

ferent results for the extent and shape of the IP in the (μ, M_0) -plane at zero temperature (see Section III) and thus an agreement of their moat regimes is not guaranteed. Moreover, while the SLAC discretization experiences a moat regime (see, e.g., right plot in Fig. 2), the non-zero positive slope of the bosonic two-point function at $q = 0$ causes our indicator Z_σ to be undefined.⁸

In this section we exclusively study Z_σ as an indicator for the moat regime. This is sufficient as for all relevant parameters within the PV and SC scheme, either $z_\sigma \leq z_{\pi_i} \leq 0$ or $z_\sigma, z_{\pi_i} \geq 0$, i.e., in the presence of a moat regime the wave-function renormalization of σ is the stronger indicator and otherwise both are positive.⁹

A. The moat regime at zero temperature

In Fig. 8 we plot the moat regime as characterized by $Z_\sigma < 0$ in the (μ, M_0) -plane at zero temperature. As in Fig. 1, the upper and the lower plot show the same data and differ only in the units used to express the chemical potential (upper in units of MeV, lower in units of the respective regulator value Λ). As for the IPs, the relevant values of the chemical potential are of the order of the regulator. For both the PV and the SC scheme, a moat regime is found in the SP adjacent to the homogeneous first order phase transition (solid line) in a large range for M_0 (roughly 250 MeV to 450 MeV for the PV scheme and 300 MeV to 450 MeV for the SC scheme). For small values of M_0 the region of negative Z_σ starts to disconnect from the HBP. The shape of the moat regime in the (μ, M_0) -plane is rather similar in both cases despite the large chemical potential (in units of the respective regulator). In contrast, the instability region boundaries (dashed lines in Fig. 8) representing the IP in both schemes are of completely different shape. This suggests that the moat regime might be a more robust feature of the NJL phase diagram in the (μ, M_0) -plane when varying the respective regulator value and changing the RS. Only for values of M_0 , which are smaller than 200 MeV, i.e., values significantly below those suggested by QCD, one does not obtain negative Z_σ for moderate values of $\mu \approx 300 \text{ MeV}$. For these small values of M_0 , however, one finds a moat regime at larger values of μ , disconnected from the HBP, which is most likely a regulator artifact.¹⁰

⁸ The indicator Z is the curvature of the bosonic two-point function at $q = 0$ (see Eq. (10)), which is an even function in q . Thus, a non-zero positive slope causes a diverging curvature at $q = 0$.

⁹ This can – in parts – be inferred from considering the respective formulae Eqs. (D1) to (D6) and was also confirmed numerically.

¹⁰ This is similar to the disconnected inhomogeneous continent, that was identified as a likely regularization artifact [88].

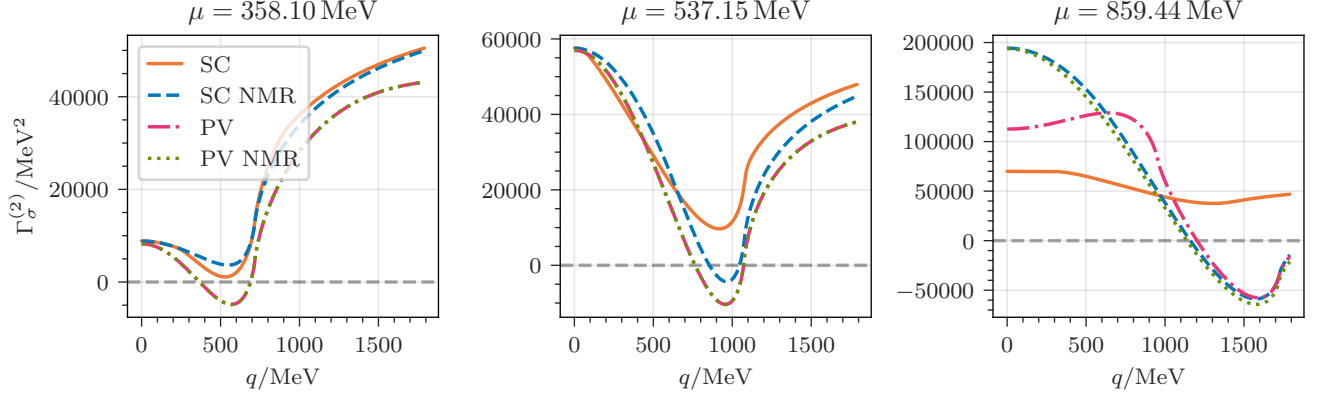


FIG. 6. The bosonic two-point function $\Gamma_\sigma^{(2)}$ as a function of the bosonic momentum q for three different values of the chemical potential μ , $T = 0$ and $M_0 = 350$ MeV within the PV and the SC scheme with and without NMR. For $\mu < \Lambda_{\text{PV}}$ (as it is the case in the left and middle plot), the two-point function with the PV scheme is unaffected by the NMR procedure. The black crosses in Fig. 7 mark the points in the (M_0, μ) -plane these plots correspond to (the position of the most right plot in the (M_0, μ) -plane is outside the plot range).

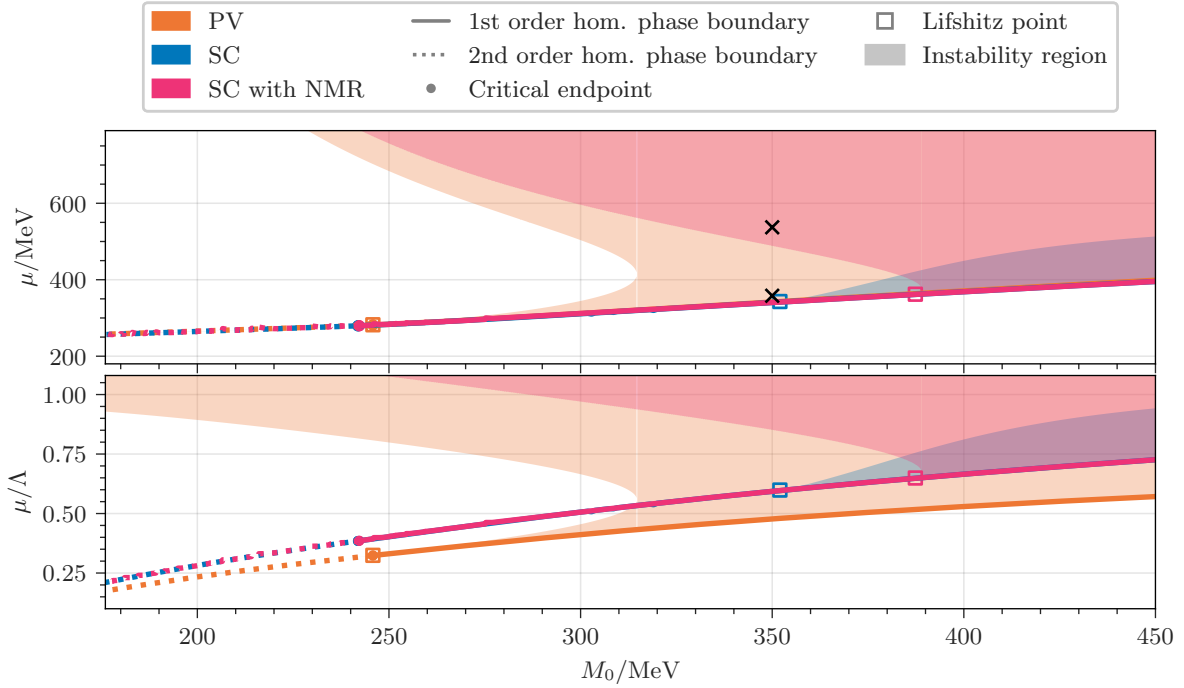


FIG. 7. The homogeneous phase diagram and the regions of instability towards an IP in the (M_0, μ) -plane at $T = 0$ for the PV and the SC scheme with and without NMR. Both plots depict the same data, but in the upper plot the chemical potential is given in units of MeV, while the lower plot gives μ in units of the respective Λ , which is a function of M_0 . The solid and dotted lines represent first and second order homogeneous phase boundaries respectively obtained by a minimization of the effective potential. The circle represents the CP that separates these boundaries. The shaded regions are the instability regions where the bosonic two-point function exhibits negative values for non-zero spatial momenta. The open squares indicate the position of the LP. The black crosses mark (M_0, μ) -values chosen for the plots in Fig. 6 (the position of the most right plot in the (M_0, μ) -plane is outside the plot range).

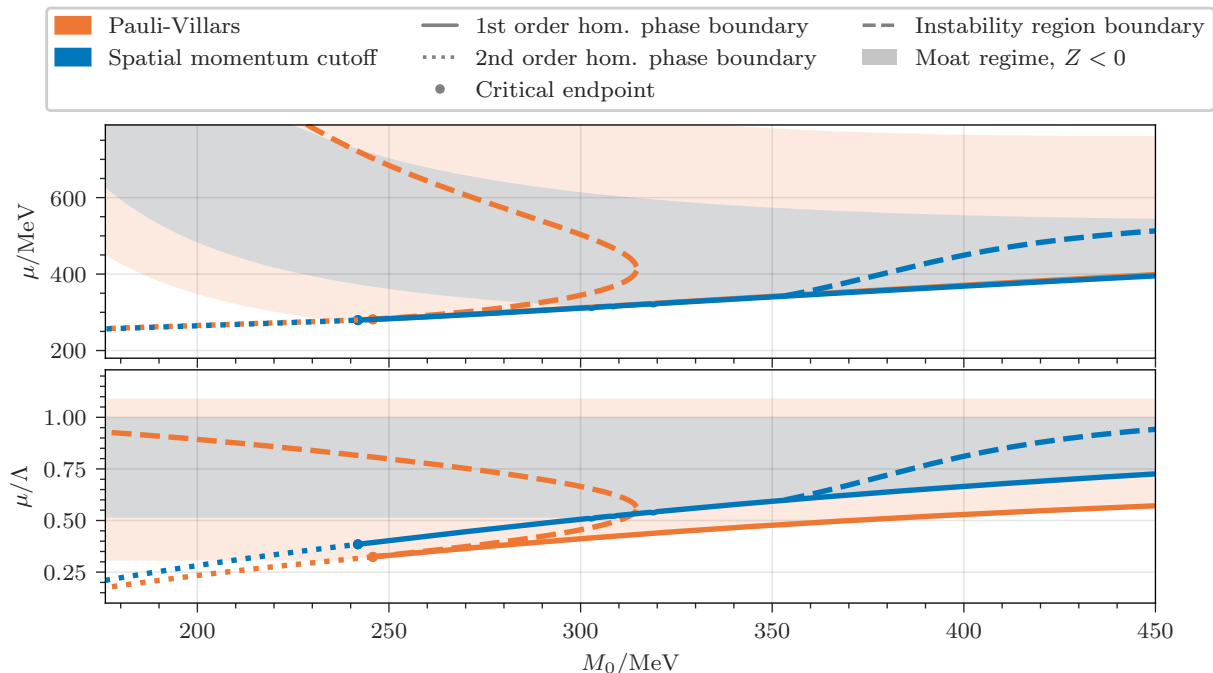


FIG. 8. Homogeneous phase boundaries, instability region boundary and the moat regime from the stability analysis at $T = 0$ in the (M_0, μ) -plane for the PV and the SC regularization. Both plots depict the same data, but in the upper plot the chemical potential is given in units of MeV, while the lower plot gives μ in units of the respective Λ , which is a function of M_0 . The solid and dotted lines represent first and second order homogeneous phase boundaries respectively obtained by a minimization of the effective potential. The circle represents the CP that separates these boundaries. The dashed lines delimit the instability regions where the bosonic two-point function exhibits negative values for non-zero spatial momenta. The shaded regions depict the moat regime, where the wave-function renormalization Z_σ is negative.

B. The moat regime at finite temperature

The moat regime appears to be a fairly stable feature of the phase diagram at zero temperature. In the following we explore, whether this is also the case for finite temperature and map out the moat regime in the (T, μ) -plane for the PV and the SC scheme. We present results for $M_0 = 400$ MeV, but the relative differences within the schemes, remain mild even for significant variations of M_0 . In Fig. 9, we plot the value of Z_σ on the right side alongside the value of the homogeneous minimum $M = \bar{\Sigma}$ in a color map on the left side for both schemes. Again, we obtain fair agreement for the moat regime within the two schemes. Starting from the $Z_\sigma = 0$ line (depicted by the dotted line), the wave function renormalization starts to decrease when increasing μ at fixed temperature. In contrast, when one starts at a fixed (μ, T) point within the moat regime, Z_σ grows with increasing T crossing the $Z_\sigma = 0$ line at a certain point. This qualitative behavior is identical within both RSs and reminds of the moat regime that is found in the $(1+1)$ -dimensional GN model [33]. In the SC scheme, the moat regime starts at a lower temperature along the homogeneous phase boundary of the HBP. This is caused by the splitting of the CP and

the LP in the SC scheme, as also obtained in the (μ, M_0) phase diagram at zero temperature and discussed in Section III A. In the PV scheme, one finds $Z_\sigma \leq 0$ adjacent to the CP in the phase diagram, as the CP coincides with the LP in this scheme [23].

In Fig. 10, the respective moat regimes of the PV and SC scheme are compared in a single plot of the (T, μ) -plane. This demonstrates again the similarity of the moat regime within the two schemes. Small differences as shown in the plot are expected, since the NJL model is an effective theory with a dependence on the regularization. This dependence should, however, be mild to consider the results a reasonably accurate phenomenological description of certain aspects of the related fundamental theory, which is QCD. As the quantitative differences concerning the moat regime within the explored schemes are indeed small, the presented results might be a hint that a moat regime of similar extent also exists in QCD. In other words, the consistent results in both the (μ, M_0) and the (T, μ) -plane with respect to the regularization suggest that the moat regime is a consequence of the action of the NJL model and not an artifact associated with the RS.

From Eq. (10), the definition of z_ϕ , and the integrals appearing in the two-point function $\Gamma^{(2)}$, one can under-

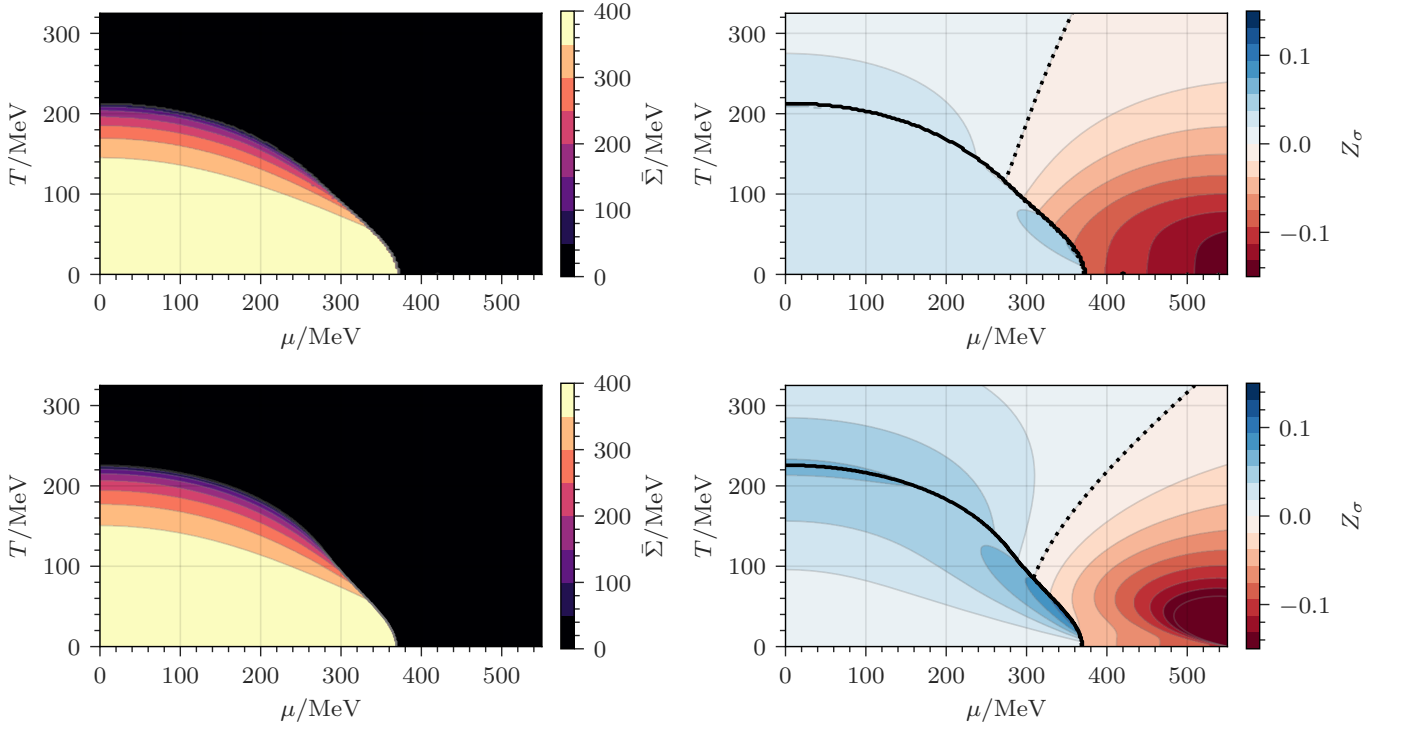


FIG. 9. The homogeneous minimum of the effective action (**left**) and the scalar-wave function renormalization (**right**) in the PV (**top**) and SC (**bottom**) scheme for $M_0 = 400$ MeV. In the right column, the dotted lines correspond to $Z_\sigma = 0$ and the solid lines indicate the location of the homogeneous phase transition.

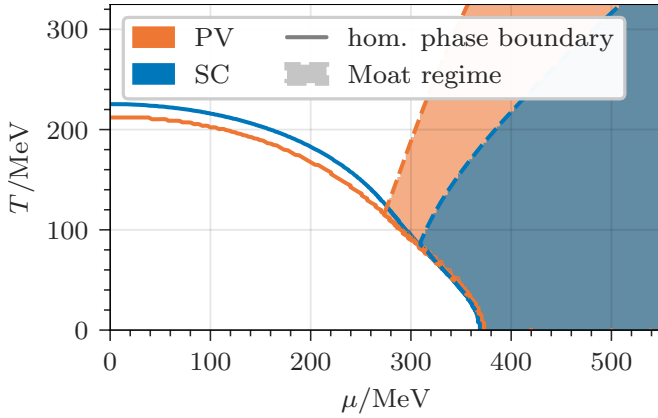


FIG. 10. Homogeneous phase boundaries and the moat regime for $M_0 = 400$ MeV for both the PV and the SC schemes.

stand, why the moat regime is more robust than predictions of an IP. z_ϕ is a quantity exclusively evaluated at $q = 0$. Thus, one expects a smaller impact from the UV regularization. In this sense, the evaluation of z_ϕ is similar to the homogeneous phase boundary, which is also located at values of the chemical potentials of the order of the regulator, but not larger, and which also does not exhibit a sizable RS dependence.

C. The wave-function renormalization at the symmetric point

The robustness of the moat regime also stems from the fact that z_ϕ is independent of the FF coupling G , but only depends on the dimensionless ratios $\bar{\sigma}/\Lambda$, T/Λ and μ/Λ , as can be seen from appropriately rescaling Eq. (D1) and Eq. (D5) with Λ . Z_σ has to be evaluated at $\bar{\sigma} = \bar{\Sigma}$, which is given by the minimization of the effective potential and thus introduces an implicit dependence on G , when it is evaluated in the HBP. In the SP and IP (where the moat regime is found, compare to Figs. 8 to 10) $\bar{\sigma} = 0$ and, consequently, $z_\sigma(\bar{\sigma} = 0) = Z_\sigma$ only depends on T/Λ and μ/Λ . This is also the reason that the boundaries of the moat regimes in Fig. 8 in the lower plot are independent of M_0 , while the boundaries of the IPs in Fig. 1 in the lower plot are a function of M_0 . We depict $z_\sigma(\bar{\sigma} = 0)$ in Fig. 11 for the PV and the SC scheme in the $(\mu/\Lambda, T/\Lambda)$ -plane. Again, we find a similar behavior of z_σ within both RSs in agreement with the previous discussion.

Of course, the region, where $\bar{\Sigma} = 0$ still depends on the respective value of the regulator Λ and the coupling G and, thus, on the selected parameters f_π and M_0 . Within this region corresponding to the SP and IP, however, the behavior of Z_σ is universal when rescaling the temperature and chemical potential by the respectively used regulator Λ . This is also an explanation for the behavior discussed in Section IV A, where the moat regime disconnects from the phase boundary to the HBP at small

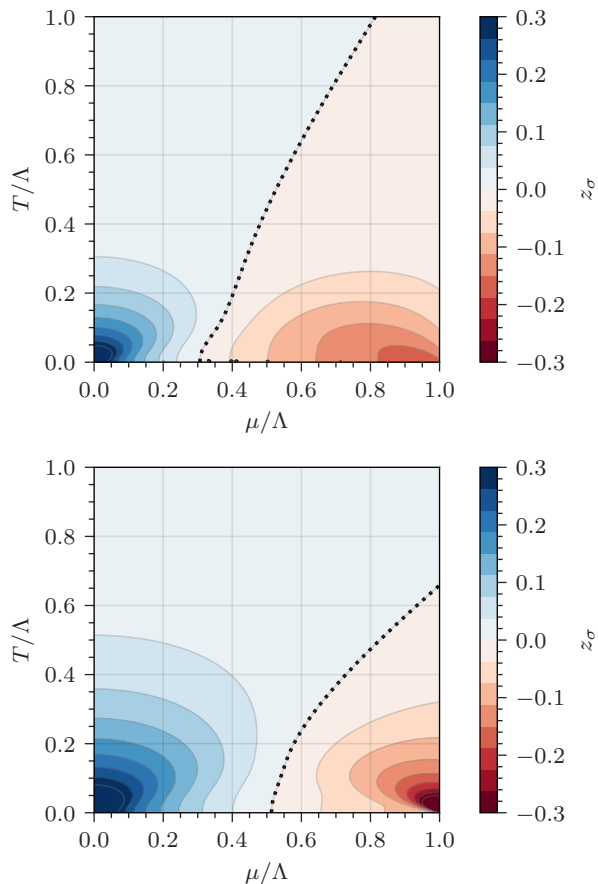


FIG. 11. The wave-function renormalization z_σ at the symmetric point $\bar{\sigma} = 0$ in the (T, μ) -plane for the PV (**top**) and the SC (**bottom**) regularization. The dotted line corresponds to the line where $z_\sigma = 0$.

values of M_0 (see Fig. 8). Such small values of M_0 correspond to large values of Λ . This causes a large scaling of Fig. 11, which effectively moves the moat regime to large chemical potentials in units of MeV.

V. CONCLUSIONS

In this work, we studied the inhomogeneous phase (IP), the moat regime and the corresponding phase diagram in the 3+1-dimensional Nambu-Jona-Lasinio (NJL) model with a particular focus on their regularization scheme (RS) dependence. We also explored the dependence on the value of the respective regulator, which implicitly controls the vacuum constituent quark mass M_0 . We fixed the pion decay constant at the physically motivated value $f_\pi = 88$ MeV and compared several common RSs at identical values of M_0 in the range $200 \text{ MeV} \lesssim M_0 \lesssim 450 \text{ MeV}$.

We found that the extent and shape of the IP in the (μ, M_0) -plane at $T = 0$ drastically differ within each of the considered RSs. For example within the Hybrid_{cos} scheme an IP does not even exist. Within the remaining

four RSs, there is not a single point in the (μ, M_0) -plane, where the RSs exhibit an IP simultaneously. These discrepancies appear in regions where the chemical potential is of the order of the regulator. In addition to that the preferred bosonic momenta inside the IPs are typically of the order of twice the respective regulator value. This facilitates strong regularization artifacts within all RSs as there is no separation of scales of the regulator and physical quantities. Such a separation of scales is, however, important and necessary for a non-renormalizable effective theory like the NJL model to exhibit a rather weak regulator dependence. Our results confirm that predictions are not stable and, consequently, not trustworthy, not even on a qualitative level, in particular considering only results from a single RS. For large regulator values, where the required separation of scales is present, an IP does not exist independent of the choice of the RS. The corresponding M_0 values are, however, too small to even crudely approximate Quantum Chromodynamics (QCD).

Furthermore, we explored the effect of no medium regularization (NMR) on the shape and extent of the IP. We found for the spatial momentum cutoff (SC) scheme with NMR (where NMR has a drastic effect) and the Pauli-Villars (PV) scheme (where NMR has no effect) a qualitative agreement in the shape of the IP in the (μ, M_0) -plane at $T = 0$. While this might be a first step towards a regulator independent result in this model, there is still no obvious physical explanation why the application of NMR should yield more trustworthy predictions for QCD than other regularization methods.¹¹

Moreover, we investigated the moat regime within the SC and PV schemes in the (μ, T) -plane for various values of M_0 . In contrast to the IP, there is fair agreement regarding the extent of the moat regime within the two schemes and it covers a large portion of the symmetric phase (SP). This indicates that the existence of the moat regime could be a rather robust feature of the phase diagram of the NJL model, largely independent of the used RS. Even though the chemical potential is again of the order of the respective regulator, the moat regime has a much weaker dependence than IPs as it is determined by the wave function renormalization, which is calculated at vanishing external bosonic momenta compared to the IP, where the relevant momenta are of the order of 2Λ .

To summarize, we have presented numerical results and theoretical arguments indicating that results on IPs in the 3 + 1-dimensional NJL model are strongly RS dependent and, thus, do not provide evidence for the existence or absence of an IP in QCD. On the other hand, the stability of the moat regime in the 3 + 1-dimensional NJL

¹¹ In the NJL model specifying the RS is part of the definition of the model. Thus, one needs robust evidence that a certain RS renders the NJL model a better effective theory for QCD in order to promote results obtained with one RS over the ones with other RSs.

model with respect to variations of the RS and the value of the regulator could indicate its existence in QCD. First evidence from Ref. [16] applying the functional renormalization group to QCD, which found a moat regime at finite μ and T , supports this conclusion.

A. Outlook

The observed RS dependence of the IP could also play a critical role in NJL model investigations of IPs with non-vanishing magnetic fields [26–28], under rotation [94, 95] or in nuclear matter models [96, 97]. Also in these scenarios, it is important to carefully consider and study different RSs and their influence on the phase diagram. In order to make robust statements regarding the IP using NJL-type models, one would need to figure out which RS renders the NJL model the best description of finite-density QCD. This, however, should be guided by finite density QCD phenomenology, for which unfortunately little evidence exists.

To solidify the finding that the moat regime is a robust feature of the NJL model, a first step would be to study the moat regime with further RSs. Also more elaborate model approaches such as, e.g., the Polyakov-loop quark-meson model, are suitable to collect more evidence for the existence of the moat regime in finite-

density QCD. If one concludes, that it is indeed a universal behavior of strongly-interacting matter, one could rely on the mesonic dispersion relations found in the moat regime for predictions of experimental signals such as in Refs. [32, 98, 99].

ACKNOWLEDGMENTS

We thank M. Buballa, H. Gholami, A. Königstein, J. Lenz, M. Mandl, G. Markó, Z. Nussinov, M. Ogilvie, R. Pisarski, F. Rennecke, S. Schindler, A. Sciarra and A. Wipf for fruitful discussions related to this work. L. P. thanks G. Endródi for valuable discussions and for his general support at the faculty of physics at the University of Bielefeld. We acknowledge the support of the *Deutsche Forschungsgemeinschaft* (DFG, German Research Foundation) through the collaborative research center transregio CRC-TR 211 “Strong-interaction matter under extreme conditions” – project number 315477589 – TRR 211. M. Wa. acknowledges support by the Heisenberg Programme of the *Deutsche Forschungsgemeinschaft* (DFG, German Research Foundation) under grant number 399217702. L.P. and M.Wi. acknowledge the support of the *Helmholtz Graduate School for Hadron and Ion Research* and of the *Giersch Foundation*.

-
- [1] M. G. Alford, A. Schmitt, K. Rajagopal, and T. Schäfer, Color superconductivity in dense quark matter, *Rev. Mod. Phys.* **80**, 1455 (2008), [arXiv:0709.4635 \[hep-ph\]](#).
- [2] L. McLerran and R. D. Pisarski, Phases of cold, dense quarks at large $N(c)$, *Nucl. Phys. A* **796**, 83 (2007), [arXiv:0706.2191 \[hep-ph\]](#).
- [3] T. Kojo, Y. Hidaka, L. McLerran, and R. D. Pisarski, Quarkyonic Chiral Spirals, *Nucl. Phys. A* **843**, 37 (2010), [arXiv:0912.3800 \[hep-ph\]](#).
- [4] T.-G. Lee, E. Nakano, Y. Tsue, T. Tatsumi, and B. Friman, Landau-Peierls instability in a Fulde-Ferrell type inhomogeneous chiral condensed phase, *Phys. Rev. D* **92**, 034024 (2015), [arXiv:1504.03185 \[hep-ph\]](#).
- [5] Y. Hidaka, K. Kamikado, T. Kanazawa, and T. Noumi, Phonons, pions and quasi-long-range order in spatially modulated chiral condensates, *Phys. Rev. D* **92**, 034003 (2015), [arXiv:1505.00848 \[hep-ph\]](#).
- [6] S. Nakamura, H. Ooguri, and C.-S. Park, Gravity Dual of Spatially Modulated Phase, *Phys. Rev. D* **81**, 044018 (2010), [arXiv:0911.0679 \[hep-th\]](#).
- [7] H. Ooguri and C.-S. Park, Holographic End-Point of Spatially Modulated Phase Transition, *Phys. Rev. D* **82**, 126001 (2010), [arXiv:1007.3737 \[hep-th\]](#).
- [8] H. Ooguri and C.-S. Park, Spatially Modulated Phase in Holographic Quark-Gluon Plasma, *Phys. Rev. Lett.* **106**, 061601 (2011), [arXiv:1011.4144 \[hep-th\]](#).
- [9] T. Demircik, N. Jokela, M. Jarvinen, and A. Piispa, Is holographic quark-gluon plasma homogeneous?, (2024), [arXiv:2405.02392 \[hep-ph\]](#).
- [10] J. Cruz Rojas, T. Demircik, and M. Järvinen, Modulated instabilities and the AdS_2 point in dense holographic matter, (2024), [arXiv:2405.02399 \[hep-th\]](#).
- [11] Y. Aoki, G. Endrodi, Z. Fodor, S. D. Katz, and K. K. Szabo, The order of the quantum chromodynamics transition predicted by the standard model of particle physics, *Nature* **443**, 675 (2006), [arxiv:hep-lat/0611014](#).
- [12] S. Borsányi, Z. Fodor, J. N. Guenther, R. Kara, P. Parotto, A. Pásztor, and C. H. Wong, Finite volume effects near the chiral crossover (2024), [arxiv:2401.01169 \[hep-lat\]](#).
- [13] R. Bellwied, S. Borsanyi, Z. Fodor, J. Günther, S. D. Katz, C. Ratti, and K. K. Szabo, The QCD phase diagram from analytic continuation (2015), [arxiv:1507.07510 \[hep-lat, physics:hep-ph, physics:nucl-th\]](#).
- [14] A. Bazavov *et al.*, Chiral crossover in QCD at zero and non-zero chemical potentials, *Phys. Lett. B* **795**, 15 (2019).
- [15] C. S. Fischer, QCD at finite temperature and chemical potential from Dyson-Schwinger equations, *Progress in Particle and Nuclear Physics* **105**, 1 (2019), [arxiv:1810.12938 \[hep-lat, physics:hep-ph, physics:nucl-th\]](#).
- [16] W.-j. Fu, J. M. Pawłowski, and F. Rennecke, The QCD phase structure at finite temperature and density, *Physical Review D* **101**, 054032 (2020), [arxiv:1909.02991](#).
- [17] F. Gao and J. M. Pawłowski, Chiral phase structure and critical end point in QCD, *Physics Letters B* **820**, 136584 (2021), [arxiv:2010.13705 \[hep-ph, physics:hep-th\]](#).
- [18] D. A. Clarke, P. Dimopoulos, F. Di Renzo, J. Goswami,

- C. Schmidt, S. Singh, and K. Zambello, *Searching for the QCD critical point using Lee-Yang edge singularities* (2024), [arxiv:2401.08820 \[hep-lat, physics:nucl-th\]](#).
- [19] M. Buballa, NJL model analysis of quark matter at large density, *Phys. Rept.* **407**, 205 (2005), [arXiv:hep-ph/0402234](#).
- [20] B.-J. Schaefer and J. Wambach, The Phase Diagram of the Quark-Meson Model, **757**, 479, [nucl-th/0403039](#).
- [21] M. Sadzikowski and W. Broniowski, Non-uniform chiral phase in effective chiral quark models, *Physics Letters B* **488**, 63 (2000), [arxiv:hep-ph/0003282](#).
- [22] E. Nakano and T. Tatsumi, Chiral symmetry and density wave in quark matter, *Phys. Rev. D* **71**, 114006 (2005), [arXiv:hep-ph/0411350](#).
- [23] D. Nickel, Inhomogeneous phases in the Nambu-Jona-Lasino and quark-meson model, *Physical Review D* **80**, 074025 (2009), [arxiv:0906.5295](#).
- [24] S. Carignano, M. Buballa, and B.-J. Schaefer, Inhomogeneous phases in the quark-meson model with vacuum fluctuations, *Phys. Rev. D* **90**, 014033 (2014), [arXiv:1404.0057 \[hep-ph\]](#).
- [25] M. Buballa and S. Carignano, Inhomogeneous chiral condensates, *Prog. Part. Nucl. Phys.* **81**, 39 (2015), [arXiv:1406.1367 \[hep-ph\]](#).
- [26] E. J. Ferrer and V. de la Incera, Absence of Landau-Peierls Instability in the Magnetic Dual Chiral Density Wave Phase of Dense QCD, *Phys. Rev. D* **102**, 014010 (2020), [arXiv:1902.06810 \[nucl-th\]](#).
- [27] W. Gyory and V. de la Incera, Phase transitions and resilience of the magnetic dual chiral density wave phase at finite temperature and density, *Phys. Rev. D* **106**, 016011 (2022), [arXiv:2203.14209 \[nucl-th\]](#).
- [28] E. J. Ferrer, W. Gyory, and V. de la Incera, Thermal phonon fluctuations and stability of the magnetic dual chiral density wave phase in dense QCD, (2023), [arXiv:2307.05621 \[nucl-th\]](#).
- [29] D. Müller, M. Buballa, and J. Wambach, Dyson-Schwinger study of chiral density waves in QCD, *Phys. Lett. B* **727**, 240 (2013), [arXiv:1308.4303 \[hep-ph\]](#).
- [30] T. F. Motta, J. Bernhardt, M. Buballa, and C. S. Fischer, Toward a stability analysis of inhomogeneous phases in QCD, *Phys. Rev. D* **108**, 114019 (2023), [arXiv:2306.09749 \[hep-ph\]](#).
- [31] T. F. Motta, J. Bernhardt, M. Buballa, and C. S. Fischer, Inhomogeneous instabilities at large chemical potential in a rainbow-ladder QCD model, (2024), [arXiv:2406.00205 \[hep-ph\]](#).
- [32] R. D. Pisarski and F. Rennecke, Signatures of Moat Regimes in Heavy-Ion Collisions, *Physical Review Letters* **127**, 152302 (2021), [arxiv:2103.06890](#).
- [33] A. Koenigstein, L. Pannullo, S. Rechenberger, M. Winstel, and M. J. Steil, Detecting inhomogeneous chiral condensation from the bosonic two-point function in the $(1 + 1)$ -dimensional Gross-Neveu model in the mean-field approximation, *Journal of Physics A: Mathematical and Theoretical* **55**, 375402 (2022), [arxiv:2112.07024 \[cond-mat, physics:hep-ph, physics:nucl-th\]](#).
- [34] J. Lenz, L. Pannullo, M. Wagner, B. Wellegehausen, and A. Wipf, Inhomogeneous phases in the Gross-Neveu model in $1+1$ dimensions at finite number of flavors, *Physical Review D* **101**, 094512 (2020).
- [35] J. J. Lenz, L. Pannullo, M. Wagner, B. Wellegehausen, and A. Wipf, Baryons in the Gross-Neveu model in $1+1$ dimensions at finite number of flavors, *Physical Review D* **102**, 114501 (2020), [arxiv:2007.08382](#).
- [36] J. Stoll, N. Zorbach, A. Koenigstein, M. J. Steil, and S. Rechenberger, Bosonic fluctuations in the $(1 + 1)$ -dimensional Gross-Neveu(-Yukawa) model at varying μ and T and finite N , (2021), [arXiv:2108.10616 \[hep-ph\]](#).
- [37] J. J. Lenz, M. Mandl, and A. Wipf, *Physical Review D* **105**, 034512 (2022), [arxiv:2109.05525 \[cond-mat, physics:hep-lat, physics:hep-th\]](#).
- [38] R. Ciccone, L. Di Pietro, and M. Serone, Inhomogeneous Phase of the Chiral Gross-Neveu Model, *Phys. Rev. Lett.* **129**, 071603 (2022), [arXiv:2203.07451 \[hep-th\]](#).
- [39] R. Ciccone, L. Di Pietro, and M. Serone, Anomalies and Persistent Order in the Chiral Gross-Neveu model, (2023), [arXiv:2312.13756 \[hep-th\]](#).
- [40] K. Kolehmainen and G. Baym, Pion condensation at finite temperature. 2. Simple Models including thermal excitations of the pion field, *Nucl. Phys. A* **382**, 528 (1982).
- [41] O. Akerlund, P. de Forcrand, and T. Rindlisbacher, Oscillating propagators in heavy-dense QCD, *JHEP* **10**, 055, [arXiv:1602.02925 \[hep-lat\]](#).
- [42] M. A. Schindler, S. T. Schindler, L. Medina, and M. C. Ogilvie, Universality of Pattern Formation, *Phys. Rev. D* **102**, 114510 (2020), [arXiv:1906.07288 \[hep-lat\]](#).
- [43] R. D. Pisarski, A. M. Tsvelik, and S. Valgushev, How transverse thermal fluctuations disorder a condensate of chiral spirals into a quantum spin liquid, *Phys. Rev. D* **102**, 016015 (2020), [arXiv:2005.10259 \[hep-ph\]](#).
- [44] M. Haensch, F. Rennecke, and L. von Smekal, Medium Induced Mixing and Critical Modes in QCD, (2023), [arXiv:2308.16244 \[hep-ph\]](#).
- [45] M. Winstel, Spatially oscillating correlation functions in $(2 + 1)$ -dimensional four-fermion models: The mixing of scalar and vector modes at finite density, (2024), [arXiv:2403.07430 \[hep-ph\]](#).
- [46] M. Winstel and S. Valgushev, Lattice study of disordering of inhomogeneous condensates and the Quantum Pion Liquid in effective $O(N)$ model, in *Excited QCD 2024 Workshop* (2024) [arXiv:2403.18640 \[hep-lat\]](#).
- [47] E. Witten, Chiral Symmetry, the $1/n$ Expansion, and the $SU(N)$ Thirring Model, *Nucl. Phys. B* **145**, 110 (1978).
- [48] V. Melin, Y. Sekiguchi, P. Wiegmann, and K. Zarembo, Peierls Transition in Gross-Neveu Model from Bethe Ansatz, (2024), [arXiv:2404.07307 \[hep-th\]](#).
- [49] J. J. Lenz, M. Mandl, and A. Wipf, Magnetized $(2+1)$ -dimensional Gross-Neveu model at finite density, *Phys. Rev. D* **108**, 074508 (2023), [arXiv:2304.14812 \[hep-lat\]](#).
- [50] M. Buballa, L. Kurth, M. Wagner, and M. Winstel, Regulator dependence of inhomogeneous phases in the $2+1$ -dimensional Gross-Neveu model, *Physical Review D* **103** (2021), [arxiv:2012.09588](#).
- [51] R. Narayanan, Phase diagram of the large N Gross-Neveu model in a finite periodic box, *Phys. Rev. D* **101**, 096001 (2020), [arXiv:2001.09200 \[hep-th\]](#).
- [52] L. Pannullo and M. Winstel, Absence of inhomogeneous chiral phases in $2+1$ -dimensional four-fermion and Yukawa models, *Physical Review D* **108**, 036011 (2023), [arxiv:2305.09444 \[cond-mat, physics:hep-ph, physics:nucl-th\]](#).
- [53] T. L. Partyka and M. Sadzikowski, Phase diagram of the non-uniform chiral condensate in different regularization schemes at $T=0$, *J. Phys. G* **36**, 025004 (2009), [arXiv:0811.4616 \[hep-ph\]](#).
- [54] A. E. B. Pasqualotto, R. L. S. Farias, W. R. Tavares, S. S. Avancini, and G. a. Krein, Causality violation and

- the speed of sound of hot and dense quark matter in the Nambu–Jona-Lasinio model, *Phys. Rev. D* **107**, 096017 (2023), [arXiv:2301.10721 \[hep-ph\]](#).
- [55] M. Asakawa and K. Yazaki, Chiral Restoration at Finite Density and Temperature, *Nucl. Phys. A* **504**, 668 (1989).
- [56] A. Heinz, F. Giacosa, M. Wagner, and D. H. Rischke, Inhomogeneous condensation in effective models for QCD using the finite-mode approach, *Phys. Rev. D* **93**, 014007 (2016), [arXiv:1508.06057 \[hep-ph\]](#).
- [57] C. A. Islam, An NJL model analysis of a magnetised nonextensive QCD medium, (2023), [arXiv:2311.14420 \[hep-ph\]](#).
- [58] G. Basar and G. V. Dunne, Self-consistent crystalline condensate in chiral Gross-Neveu and Bogoliubov-de Gennes systems, *Physical Review Letters* **100**, 200404 (2008), [arxiv:0803.1501 \[hep-th\]](#).
- [59] G. Basar and G. V. Dunne, A Twisted Kink Crystal in the Chiral Gross-Neveu model, *Physical Review D* **78**, 065022 (2008), [arxiv:0806.2659 \[cond-mat, physics:hep-lat, physics:hep-th, physics:math-ph\]](#).
- [60] G. Basar, G. V. Dunne, and M. Thies, Inhomogeneous Condensates in the Thermodynamics of the Chiral NJL₂ model, *Physical Review D* **79**, 105012 (2009), [arxiv:0903.1868 \[cond-mat, physics:hep-lat, physics:hep-ph, physics:hep-th\]](#).
- [61] J. I. Kapusta and C. Gale, *Finite-temperature field theory: Principles and applications*, Cambridge Monographs on Mathematical Physics (Cambridge University Press, 2011).
- [62] A. Wipf, *Statistical approach to quantum field theory: An introduction*, Vol. 864 (Springer, Heidelberg, 2013).
- [63] A. Koenigstein and L. Pannullo, Inhomogeneous condensation in the Gross-Neveu model in noninteger spatial dimensions $1 \leq d < 3$. II. Nonzero temperature and chemical potential, *Phys. Rev. D* **109**, 056015 (2024), [arXiv:2312.04904 \[hep-ph\]](#).
- [64] L. Pannullo, Inhomogeneous condensation in the Gross-Neveu model in noninteger spatial dimensions $1 \leq d < 3$, *Phys. Rev. D* **108**, 036022 (2023), [arXiv:2306.16290 \[hep-ph\]](#).
- [65] L. Pannullo, M. Wagner, and M. Winstel, Inhomogeneous phases in the chirally imbalanced 2+1-dimensional Gross-Neveu model and their absence in the continuum limit, *Symmetry* **14**, 265 (2022), [arxiv:2112.11183](#).
- [66] M. Buballa, S. Carignano, and L. Kurth, Inhomogeneous phases in the quark-meson model with explicit chiral-symmetry breaking, *The European Physical Journal Special Topics* **229**, 3371 (2020), [arxiv:2006.02133](#).
- [67] M. Buballa and S. Carignano, Inhomogeneous chiral phases away from the chiral limit, *Physics Letters* **B791**, 361 (2019), [arxiv:1809.10066 \[hep-ph\]](#).
- [68] R.-A. Tripolt, B.-J. Schaefer, L. von Smekal, and J. Wambach, The low-temperature behavior of the quark-meson model, *Physical Review D* **97**, 034022 (2018), [arxiv:1709.05991 \[hep-ph, physics:hep-th, physics:nucl-th\]](#).
- [69] J. Braun, S. Finkbeiner, F. Karbstein, and D. Roscher, On the Search for Inhomogeneous Phases in Fermionic Models, [arXiv:1410.8181 \[cond-mat, physics:hep-ph, physics:nucl-th\]](#) (2014), [arxiv:1410.8181](#).
- [70] J. Braun, F. Karbstein, S. Rechenberger, and D. Roscher, Crystalline ground states in Polyakov-loop extended Nambu–Jona-Lasinio models, *Physical Review D* **93**, 014032 (2016), [arxiv:1510.04012 \[hep-ph\]](#).
- [71] A. Koenigstein and M. Winstel, Revisiting the spatially inhomogeneous condensates in the (1 + 1)-dimensional chiral Gross-Neveu model via the bosonic two-point function in the infinite- N limit, (2024), [arXiv:2405.03459 \[hep-th\]](#).
- [72] H. G. Dobereiner and P. G. Reinhard, INSTABILITIES IN THE NONLINEAR RELATIVISTIC MEAN FIELD MODEL, *Phys. Lett. B* **227**, 305 (1989).
- [73] S. P. Klevansky, The Nambu–Jona-Lasinio model of quantum chromodynamics, *Reviews of Modern Physics* **64**, 649 (1992).
- [74] P. Adhikari and J. O. Andersen, Consistent regularization and renormalization in models with inhomogeneous phases, *Physical Review D* **95**, 036009 (2017), [arxiv:1608.01097](#).
- [75] R. C. Pereira, J. a. Moreira, P. Costa, and C. Providência, A new approach to the 3-momentum regularization of the in-medium one and two fermion line integrals with applications to cross sections in the Nambu–Jona-Lasinio model, (2023), [arXiv:2310.05749 \[hep-ph\]](#).
- [76] S. D. Drell, M. Weinstein, and S. Yankielowicz, Variational approach to strong coupling field theory. I. Φ^{*4} theory, *Physical Review D* **14**, 487 (1976).
- [77] S. D. Drell, M. Weinstein, and S. Yankielowicz, Strong-coupling field theories. II. Fermions and gauge fields on a lattice, *Physical Review D* **14**, 1627 (1976).
- [78] L. H. Karsten and J. Smit, The vacuum polarization with SLAC lattice fermions, **85B**, 100.
- [79] B. H. Wellegehausen, D. Schmidt, and A. Wipf, Critical flavor number of the Thirring model in three dimensions, *Physical Review D* **96**, 094504 (2017), [arxiv:1708.01160 \[hep-lat\]](#).
- [80] J. Lenz, B. Wellegehausen, and A. Wipf, Absence of chiral symmetry breaking in Thirring models in 1+2 dimensions, *Physical Review D* **100**, 054501 (2019), [arxiv:1905.00137](#).
- [81] S. Hands and D. N. Walters, Numerical portrait of a relativistic BCS gapped superfluid, *Phys. Rev. D* **69**, 076011 (2004), [arXiv:hep-lat/0401018](#).
- [82] Y. Cohen, S. Elitzur, and E. Rabinovici, A Monte-Carlo study of the Gross-Neveu model, *Nucl. Phys. B* **220**, 102 (1983).
- [83] H. Kohyama, D. Kimura, and T. Inagaki, Regularization dependence on phase diagram in Nambu–Jona-Lasinio model, *Nucl. Phys. B* **896**, 682 (2015).
- [84] J. Braun, M. Leonhardt, and J. M. Pawłowski, Renormalization group consistency and low-energy effective theories, *SciPost Phys.* **6**, 056 (2019).
- [85] Particle Data Group, Review of Particle Physics, *Progress of Theoretical and Experimental Physics* **2022**, 083C01 (2022).
- [86] J. Gasser and H. Leutwyler, Chiral perturbation theory: Expansions in the mass of the strange quark, **250**, 465.
- [87] P. Gerber and H. Leutwyler, Hadrons below the chiral phase transition, **321**, 387.
- [88] S. Carignano and M. Buballa, Inhomogeneous islands and continents in the Nambu–Jona-Lasinio model, *Acta Phys. Polon. Supp.* **5**, 641 (2012), [arXiv:1111.4400 \[hep-ph\]](#).
- [89] S. Carignano, D. Nickel, and M. Buballa, Influence of vector interaction and Polyakov loop dynamics on inhomogeneous chiral symmetry breaking phases, *Physical Review D* **82**, 054009 (2010), [arxiv:1007.1397 \[hep-ph\]](#).

- [90] S. Carignano, M. Schramm, and M. Buballa, Influence of vector interactions on the favored shape of inhomogeneous chiral condensates, *Physical Review D* **98**, 014033 (2018), arXiv:1805.06203 [hep-ph].
- [91] L. Pannullo, *Inhomogeneous phases and the Moat Regime in Nambu-Jona-Lasinio-Type models*, Ph.D. thesis, Frankfurt U. (2024).
- [92] S. Carignano and M. Buballa, Two-dimensional chiral crystals in the NJL model, *Phys. Rev. D* **86**, 074018 (2012), arXiv:1203.5343 [hep-ph].
- [93] T. D. Cohen, Functional integrals for QCD at nonzero chemical potential and zero density, *Phys. Rev. Lett.* **91**, 222001 (2003), arXiv:hep-ph/0307089.
- [94] S. M. A. Tabatabaee Mehr, Chiral symmetry breaking and phase diagram of dual chiral density wave in a rotating quark matter, *Phys. Rev. D* **108**, 094042 (2023), arXiv:2306.11753 [nucl-th].
- [95] S. Chen, K. Fukushima, and Y. Shimada, Inhomogeneous confinement and chiral symmetry breaking induced by imaginary angular velocity, (2024), arXiv:2404.00965 [hep-ph].
- [96] K. Takahashi and T. Tatsumi, Sigma pi0 condensation at finite density in the linear sigma model, *Phys. Rev. C* **63**, 015205 (2001).
- [97] S. Pitsinikos and A. Schmitt, Chiral crossover versus chiral density wave in dense nuclear matter, *Phys. Rev. D* **109**, 014024 (2024), arXiv:2309.01603 [nucl-th].
- [98] F. Rennecke, R. D. Pisarski, and D. H. Rischke, Particle interferometry in a moat regime, *Phys. Rev. D* **107**, 116011 (2023).
- [99] K. Fukushima, Y. Hidaka, K. Inoue, K. Shigaki, and Y. Yamaguchi, Hanbury-Brown–Twiss signature for clustered substructures probing primordial inhomogeneity in hot and dense QCD matter, *Phys. Rev. C* **109**, L051903 (2024), arXiv:2306.17619 [hep-ph].

Appendix A: Parameter fitting

In this appendix, we discuss how the parameters G and Λ in the NJL model (see the discussion in the last paragraph of Section II A and in Section IID) are fitted to the constituent quark mass M_0 and the pion decay constant f_π in the vacuum. We use the gap equation (9) to relate G to the ratio M_0/Λ and the vacuum-to-one-pion axial vector matrix element to express f_π/M_0 as a function of M_0/Λ , as proposed in Ref. [73]. These two relations itself and, consequently, the solution for G and Λ depends on the respective RS. In the following, we present the relevant expressions for this computation for each of the five used RSs.

1. Pauli-Villars

Computing the vacuum-to-one-pion axial vector matrix element yields

$$\frac{f_\pi^2}{M_0^2} = -\frac{\bar{N}}{8\pi^2} \sum_{k=0}^{N_{PV}} c_k \ln \left(\frac{M_{0,k}^2}{\Lambda_{PV}^2} \right), \quad (\text{A1})$$

while the gap equation (9) gives

$$\frac{1}{G} = \frac{\bar{N}}{8\pi^2} \sum_{k=0}^{N_{PV}} c_k M_{0,k}^2 \ln \left(\frac{M_{0,k}^2}{\Lambda_{PV}^2} \right), \quad (\text{A2})$$

where $M_{0,k}^2 = M_0^2 + \alpha_k \Lambda_{PV}^2$. See below Eq. (1) for the definition of \bar{N} .

2. Spatial Momentum Cutoff

For the spatial momentum cutoff, we find

$$\frac{f_\pi^2}{M_0^2} = \frac{\bar{N}}{16\pi^2} \left[\operatorname{arsinh} \left(\frac{\Lambda_{SC}}{|M_0|} \right) - \left(\frac{M_0^2}{\Lambda_{SC}^2} + 1 \right)^{-\frac{1}{2}} \right], \quad (\text{A3})$$

and

$$\frac{1}{G} = \frac{\bar{N}}{4\pi^2} \left[\Lambda_{SC} \sqrt{M_0^2 + \Lambda_{SC}^2} - \operatorname{arsinh} \left(\frac{\Lambda_{SC}}{|M_0|} \right) M_0^2 \right], \quad (\text{A4})$$

respectively.

3. Lattice Regularization

The formulas for the lattice regularizations differ exclusively in their expression for the energy E (see Eq. (A7)). Therefore, we do not need to distinguish between the SLAC and Hybrid discretization here. The quantities of the parameter fitting are given by

$$\frac{f_\pi^2}{M_0^2} = \frac{\bar{N}}{4\pi^4} \int_0^{\Lambda_{LFT}} dp_1 \int_0^{\Lambda_{LFT}} dp_2 \int_0^{\Lambda_{LFT}} dp_3 \times \left[\frac{\arctan \left(\frac{\Lambda_{LFT}}{E} \right)}{E^3} + \frac{\Lambda_{LFT}}{E^2(E^2 + \Lambda_{LFT}^2)} \right] \quad (\text{A5})$$

and

$$\frac{1}{G} = \frac{2\bar{N}}{\pi^4} \int_0^{\Lambda_{LFT}} dp_1 \int_0^{\Lambda_{LFT}} dp_2 \int_0^{\Lambda_{LFT}} dp_3 \frac{1}{E} \arctan \left(\frac{E}{\Lambda_{LFT}} \right). \quad (\text{A6})$$

The energies for the respective lattice regularization are

$$E = \sqrt{\sum_{i=1}^3 \mathcal{P}_X^2(p_i) + \bar{\sigma}^2} \quad (\text{A7})$$

where \mathcal{P}_{SLAC} is defined in Eq. (17) and

$$\mathcal{P}_{Hybrid}(p_\mu) = \delta_{\mu,0} \mathcal{P}_{SLAC}(p_0) + \delta_{\mu,j} \sin(\mathbf{p}_j a). \quad (\text{A8})$$

Appendix B: Homogeneous effective potential

Here, we give the relevant expressions for the evaluation of the homogeneous effective potential (8) by specifying l_0 for each of the five RSs used. The unregularized and therefore divergent expression is given by

$$l_0(\bar{\sigma}, T, \mu) = \frac{1}{2\pi^2} \int_0^\infty dp p^2 \left[E + \frac{1}{\beta} \ln \left(1 + e^{-\beta(E+\mu)} \right) + \frac{1}{\beta} \ln \left(1 + e^{-\beta(E-\mu)} \right) \right] \quad (\text{B1})$$

with $E = \sqrt{p^2 + \bar{\sigma}^2}$.

1. Pauli-Villars

For arbitrary $\bar{\sigma}, T, \mu$, one finds

$$\begin{aligned} l_0(\bar{\sigma}, T, \mu) &= \frac{1}{2\pi^2} \int_0^\infty dp p^2 \sum_{k=0}^{N_{\text{PV}}} c_k \left[E_k + \frac{1}{\beta} \ln \left(1 + e^{-\beta(E_k+\mu)} \right) + \frac{1}{\beta} \ln \left(1 + e^{-\beta(E_k-\mu)} \right) \right] = \\ &= \frac{1}{32\pi^2} \left\{ \sum_{k=0}^{N_{\text{PV}}} c_k M_k^4 \ln \left(\frac{M_k^2}{\Lambda_{\text{PV}}^2} \right) + 16 \int_0^\infty dp \frac{p^4}{3} \sum_{k=0}^{N_{\text{PV}}} c_k \frac{n(E_k) + \bar{n}(E_k)}{E_k} \right\}, \end{aligned} \quad (\text{B2})$$

where we used partial integration and defined the Fermi-Dirac distribution functions

$$n(x) = \frac{1}{1 + e^{\beta(x-\mu)}}, \quad \bar{n}(x) = \frac{1}{1 + e^{\beta(x+\mu)}}. \quad (\text{B3})$$

For $\mu = T = 0$, we find

$$l_0(\bar{\sigma}, T = 0, \mu = 0) = \frac{1}{32\pi^2} \sum_{k=0}^{N_{\text{PV}}} c_k M_k^4 \ln \left(\frac{M_k^2}{\Lambda_{\text{PV}}^2} \right) \quad (\text{B4})$$

implying

$$l_0(\bar{\sigma} = 0, T = 0, \mu = 0) = \frac{\Lambda_{\text{PV}}^4}{32\pi^2} \sum_{k=1}^{N_{\text{PV}}} c_k \alpha_k^2 \ln(\alpha_k). \quad (\text{B5})$$

using that $M_k = \alpha_k$ for $\bar{\sigma} = 0$. Moreover, we find

$$l_0(\bar{\sigma}, T = 0, \mu) = \frac{1}{32\pi^2} \sum_{k=0}^{N_{\text{PV}}} c_k \left\{ M_k^4 \ln \left(\frac{M_k^2}{\Lambda_{\text{PV}}^2} \right) + \Theta(\bar{\mu}_k^2) \frac{2}{3} \left[3M_k^2 \operatorname{arsinh} \left(\frac{\bar{\mu}_k}{|M_k|} \right) + \bar{\mu}_k \left(2|\mu|^3 - 5M_k^2 |\mu| \right) \right] \right\}, \quad (\text{B6})$$

and

$$\begin{aligned} l_0(\bar{\sigma} = 0, T = 0, \mu) &= \frac{1}{32\pi^2} \left\{ \Lambda_{\text{PV}}^4 \sum_{k=1}^{N_{\text{PV}}} c_k \alpha_k^2 \ln(\alpha_k) + \Theta(\mu^2) \frac{4\mu^4}{3} + \right. \\ &\quad \left. + \sum_{k=1}^{N_{\text{PV}}} c_k \Theta(\bar{\mu}_k^2) \frac{2}{3} \left[3M_k^2 \operatorname{arsinh} \left(\frac{\bar{\mu}_k}{|M_k|} \right) + \bar{\mu}_k \left(2|\mu|^3 - 5M_k^2 \mu \right) \right] \right\}, \end{aligned} \quad (\text{B7})$$

where

$$\bar{\mu}_k = \sqrt{\mu^2 - M_k^2}. \quad (\text{B8})$$

2. Spatial Momentum Cutoff

For the SC scheme, one obtains

$$\begin{aligned}
l_0(\bar{\sigma}, T, \mu) &= \frac{1}{2\pi^2} \int_0^{\Lambda_{\text{SC}}} dp p^2 \left[E + \frac{1}{\beta} \ln \left(1 + e^{-\beta(E+\mu)} \right) + \frac{1}{\beta} \ln \left(1 + e^{-\beta(E-\mu)} \right) \right] = \\
&= \frac{1}{16\pi^2} \left\{ \Lambda_{\text{SC}} \sqrt{\Lambda_{\text{SC}}^2 + \bar{\sigma}^2} (2\Lambda_{\text{SC}}^2 + \bar{\sigma}^2) - \bar{\sigma}^4 \operatorname{arsinh} \left(\frac{\Lambda_{\text{SC}}}{|\bar{\sigma}|} \right) + \right. \\
&\quad \left. + 8 \int_0^{\Lambda_{\text{SC}}} dp p^2 \left[\frac{1}{\beta} \ln \left(1 + e^{-\beta(E+\mu)} \right) + \frac{1}{\beta} \ln \left(1 + e^{-\beta(E-\mu)} \right) \right] \right\}. \tag{B9}
\end{aligned}$$

For $\mu = T = 0$, one finds the closed form expression

$$l_0(\bar{\sigma}, T = 0, \mu = 0) = \frac{1}{16\pi^2} \left[\Lambda_{\text{SC}} \sqrt{\Lambda_{\text{SC}}^2 + \bar{\sigma}^2} (2\Lambda_{\text{SC}}^2 + \bar{\sigma}^2) - \bar{\sigma}^4 \operatorname{arsinh} \left(\frac{\Lambda_{\text{SC}}}{|\bar{\sigma}|} \right) \right] \tag{B10}$$

which reduces to

$$l_0(\bar{\sigma} = 0, T = 0, \mu = 0) = \frac{\Lambda_{\text{SC}}^4}{8\pi^2} \tag{B11}$$

for $\bar{\sigma} = 0$.

Moreover, one finds

$$\begin{aligned}
&l_0(\bar{\sigma}, T = 0, \mu) = \\
&= l_0(\bar{\sigma}, T = 0, \mu = 0) - \frac{\Theta(\bar{\mu}^2)}{16\pi^2} \int_0^{P=\min(\Lambda_{\text{SC}}, \bar{\mu})} dp p^2 (E - |\mu|) = \\
&= l_0(\bar{\sigma}, T = 0, \mu = 0) - \frac{\Theta(\bar{\mu}^2)}{16\pi^2} \left[P \sqrt{P^2 + \bar{\sigma}^2} (2P^2 + \bar{\sigma}^2) - \bar{\sigma}^4 \operatorname{arsinh} \left(\frac{P}{|\bar{\sigma}|} \right) - \frac{|\mu| P^3}{3} \right] = \\
&= \frac{1}{16\pi^2} \begin{cases} \Lambda_{\text{SC}} \sqrt{\Lambda_{\text{SC}}^2 + \bar{\sigma}^2} (2\Lambda_{\text{SC}}^2 + \bar{\sigma}^2) - \bar{\sigma}^4 \operatorname{arsinh} \left(\frac{\Lambda_{\text{SC}}}{|\bar{\sigma}|} \right) & \text{if } \bar{\mu} = 0, \\ \Lambda_{\text{SC}} \sqrt{\Lambda_{\text{SC}}^2 + \bar{\sigma}^2} (2\Lambda_{\text{SC}}^2 + \bar{\sigma}^2) - \bar{\sigma}^4 \operatorname{arsinh} \left(\frac{\Lambda_{\text{SC}}}{|\bar{\sigma}|} \right) \\ - \bar{\mu} |\mu|^3 + \bar{\sigma}^4 \operatorname{arsinh} \left(\frac{\bar{\mu}}{|\bar{\sigma}|} \right) + \frac{2}{3} |\mu| \bar{\mu}^3 & \text{if } 0 < \bar{\mu}^2 < \Lambda_{\text{SC}}^2, \\ \frac{|\mu| \Lambda_{\text{SC}}^3}{3} & \text{if } \bar{\mu}^2 > \Lambda_{\text{SC}}^2 \end{cases}, \tag{B12}
\end{aligned}$$

where

$$\bar{\mu} = \sqrt{\mu^2 - \bar{\sigma}^2}, \tag{B13}$$

and

$$\begin{aligned}
l_0(\bar{\sigma} = 0, T = 0, \mu) &= \frac{\Lambda_{\text{SC}}^4}{8\pi^2} - \frac{\Theta(\mu^2)}{16\pi^2} \int_0^{P=\min(\Lambda_{\text{SC}}, |\mu|)} dp p^2 (p - |\mu|) = \\
&= \frac{1}{8\pi^2} \left\{ \Lambda_{\text{SC}}^4 - \Theta(\mu^2) \left[P^4 - \frac{4}{3} |\mu| P^3 \right] \right\} = \\
&= \frac{1}{8\pi^2} \begin{cases} \Lambda_{\text{SC}}^4 & \text{if } \mu = 0, \\ \Lambda_{\text{SC}}^4 + \frac{1}{3} \mu^4 & 0 < \mu^2 \leq \Lambda_{\text{SC}}^2, \\ \frac{4}{3} |\mu| \Lambda_{\text{SC}}^3 & \mu^2 > \Lambda_{\text{SC}}^2 \end{cases}. \tag{B14}
\end{aligned}$$

3. Lattice Regularization

The formulas for the lattice regularizations differ exclusively in their expression for the energy E (see Eq. (A7)). Therefore, we do not need to distinguish between the SLAC and Hybrid discretization here. The resulting expression in the zero temperature limit is

$$l_0(\bar{\sigma}, T = 0, \mu) = \frac{8}{(2\pi)^4} \int_0^{\Lambda_{\text{LFT}}} dp_1 \int_0^{\Lambda_{\text{LFT}}} dp_2 \int_0^{\Lambda_{\text{LFT}}} dp_3 \left[-4\Lambda_{\text{LFT}} - 2|\mu| \arctan 2(2|\mu| \Lambda_{\text{LFT}}, E^2 - \mu^2 + \Lambda_{\text{LFT}}^2) + \right.$$

$$\begin{aligned}
& + 2E \arctan 2(2E\Lambda_{\text{LFT}}, E^2 - \mu^2 - \Lambda_{\text{LFT}}^2) + \Lambda_{\text{LFT}} \ln \left(4\mu^2 \Lambda_{\text{LFT}}^2 + (E^2 - \mu^2 + \Lambda_{\text{LFT}}^2)^2 \right) + \\
& - \Theta(\mu^2 - E^2) 2\pi(E - |\mu|) \Big], \tag{B15}
\end{aligned}$$

where

$$\arctan 2(y, x) = \begin{cases} \arctan\left(\frac{y}{x}\right) & \text{if } x > 0, \\ \arctan\left(\frac{y}{x}\right) + \pi & \text{if } x < 0 \text{ and } y \geq 0, \\ \arctan\left(\frac{y}{x}\right) - \pi & \text{if } x < 0 \text{ and } y < 0, \\ +\frac{\pi}{2} & \text{if } x = 0 \text{ and } y > 0, \\ -\frac{\pi}{2} & \text{if } x = 0 \text{ and } y < 0, \\ \text{undefined} & \text{if } x = 0 \text{ and } y = 0. \end{cases} \tag{B16}$$

Appendix C: Stability analysis

For the SC and PV scheme, the bosonic two-point function is split up into the q -independent part l_1 and a q -dependent part L_2 . For the two-point function of bosonic field $\phi_i = (\sigma, \boldsymbol{\pi})_i$, one finds

$$\Gamma_{\phi_i}^{(2)}(\mathbf{q}, \bar{\sigma}, \mu, T) = \frac{1}{2G} - \bar{N}l_1(\bar{\sigma}, \mu, T) + \bar{N}L_{2, \phi_i}(\mathbf{q}, \bar{\sigma}, \mu, T) \tag{C1}$$

with

$$l_1 = \int \frac{d^3 p}{(2\pi)^3} \frac{1}{\beta} \sum_{n=-\infty}^{\infty} \frac{1}{(\nu_n - i\mu)^2 + E^2} = \int \frac{d^3 p}{(2\pi)^3} \frac{1 - n(E) - \bar{n}(E)}{E} \tag{C2}$$

and

$$\begin{aligned}
L_{2, \phi_i}(\mathbf{q}, \bar{\sigma}, \mu, T) &= \int \frac{d^3 p}{(2\pi)^3} \frac{1}{\beta} \sum_{n=-\infty}^{\infty} \frac{\mathbf{p} \cdot \mathbf{q} + \mathbf{q}^2 + 2\delta_{i,0}\bar{\sigma}^2}{\left[(\nu_n - i\mu)^2 + E_{\mathbf{p}}^2 \right] \left[(\nu_n - i\mu)^2 + E_{\mathbf{p}+\mathbf{q}}^2 \right]} = \\
&= \int \frac{d^3 p}{(2\pi)^3} \frac{\mathbf{p} \cdot \mathbf{q} + \mathbf{q}^2 + 2\delta_{i,0}\bar{\sigma}^2}{\mathbf{q}^2 + 2\mathbf{p} \cdot \mathbf{q}} \times \left[\frac{1 - n(E) - \bar{n}(E)}{E} - \frac{1 - n(E_{\mathbf{p}+\mathbf{q}}) - \bar{n}(E_{\mathbf{p}+\mathbf{q}})}{E_{\mathbf{p}+\mathbf{q}}} \right]. \tag{C3}
\end{aligned}$$

1. Pauli-Villars

a. The momentum independent integral l_1

In the PV scheme, we have

$$l_1(\bar{\sigma}, \mu, T) = \frac{1}{4\pi^2} \sum_{k=0}^{N_{\text{PV}}} c_k \left\{ M_k^2 \ln \left(\frac{M_k^2}{\Lambda_{\text{PV}}^2} \right) - \int_0^\infty dp p^2 \frac{n(E_k) + \bar{n}(E_k)}{2E_k} \right\}. \tag{C4}$$

The vacuum contribution reads

$$l_1(\bar{\sigma}, \mu = 0, T = 0) = \frac{1}{4\pi^2} \sum_{k=0}^{N_{\text{PV}}} c_k M_k^2 \ln \left(\frac{M_k^2}{\Lambda_{\text{PV}}^2} \right), \tag{C5}$$

where taking $\bar{\sigma} \rightarrow 0$ yields

$$l_1(\bar{\sigma} = 0, \mu = 0, T = 0) = \frac{\Lambda_{\text{PV}}^2}{4\pi^2} \sum_{k=1}^{N_{\text{PV}}} c_k \alpha_k \ln(\alpha_k). \tag{C6}$$

At zero temperature, we find

$$l_1(\bar{\sigma}, \mu, T = 0) = \frac{1}{4\pi^2} \sum_{k=0}^{N_{\text{PV}}} c_k \left\{ M_k^2 \ln \left(\frac{M_k^2}{\Lambda_{\text{PV}}^2} \right) - \frac{\Theta(\bar{\mu}_k^2)}{2} \left[|\mu| \bar{\mu}_k - M_k^2 \operatorname{arsinh} \left(\frac{\bar{\mu}_k}{|M_k|} \right) \right] \right\} \tag{C7}$$

and for $\bar{\sigma} = 0$

$$l_1(\bar{\sigma} = 0, \mu, T = 0) = \frac{1}{4\pi^2} \left\{ \sum_{k=1}^{N_{\text{PV}}} c_k \alpha_k \ln(\alpha_k) - \Theta(\mu^2) \frac{\mu^2}{2} - \sum_{k=1}^{N_{\text{PV}}} c_k \frac{\Theta(\bar{\mu}_k^2)}{2} \left[|\mu| \bar{\mu}_k - M_k^2 \operatorname{arsinh} \left(\frac{\bar{\mu}_k}{|M_k|} \right) \right] \right\}. \quad (\text{C8})$$

b. The Momentum Dependent Integral L_2

We perform a shift in the momentum integral of L_{2,ϕ_i} and obtain

$$L_{2,\phi_i}(\mathbf{q}, \bar{\sigma}, \mu, T) = (\mathbf{q}^2 + \delta_{i,1} 4\bar{\sigma}^2) \int \frac{d^3p}{(2\pi)^3} \frac{1}{2\mathbf{p} \cdot \mathbf{q} - q^2} \frac{1 - n(E) - \bar{n}(E)}{2E} \equiv (\mathbf{q}^2 + \delta_{i,1} 4\bar{\sigma}^2) l_2(\mathbf{q}, \bar{\sigma}, \mu, T), \quad (\text{C9})$$

where only l_2 will be regulated using the PV scheme to be consistent with existing literature [24, 66]. We, thus, obtain

$$L_{2,\phi_i}(q, \bar{\sigma}, \mu, T) = -\frac{(q^2 + \delta_{i,0} 4\bar{\sigma}^2)}{(4\pi)^2} \sum_{k=0}^{N_{\text{PV}}} c_k \left\{ \left[\frac{1}{2} \ln \left(\frac{M_k^2}{\Lambda_{\text{PV}}^2} \right) + \sqrt{1 + \frac{4M_k^2}{q^2}} \operatorname{arcoth} \left(\sqrt{1 + \frac{4M_k^2}{q^2}} \right) \right] + \right. \\ \left. - \int_0^\infty dp \frac{p}{q} \frac{n(E_k) + \bar{n}(E_k)}{E_k} \ln \left| \frac{2p - q}{2p + q} \right| \right\} \quad (\text{C10})$$

and taking the zero temperature limit yields

$$L_{2,\phi_i}(q, \bar{\sigma}, \mu, T = 0) = \\ = -\frac{(q^2 + \delta_{i,0} 4\bar{\sigma}^2)}{(4\pi)^2} \sum_{k=0}^{N_{\text{PV}}} c_k \left\{ \left[\frac{1}{2} \ln \left(\frac{M_k^2}{\Lambda_{\text{PV}}^2} \right) + \sqrt{1 + \frac{4M_k^2}{q^2}} \operatorname{arcoth} \left(\sqrt{1 + \frac{4M_k^2}{q^2}} \right) \right] + \right. \\ \left. - \Theta(\bar{\mu}_k^2) \left[-\operatorname{artanh} \left(\frac{\bar{\mu}_k}{|\mu|} \right) + \frac{1}{2} \sqrt{1 + \frac{4M_k^2}{q^2}} \ln \left| \frac{q|\mu| + \bar{\mu}_k \sqrt{q^2 + 4M_k^2}}{q|\mu| - \bar{\mu}_k \sqrt{q^2 + 4M_k^2}} \right| - \frac{|\mu|}{q} \ln \left| \frac{2\bar{\mu}_k + q}{2\bar{\mu}_k - q} \right| \right] \right\}. \quad (\text{C11})$$

In the SP, one finds

$$L_{2,\phi_i}(q, \bar{\sigma} = 0, \mu, T = 0) = \\ = -\frac{q^2}{(4\pi)^2} \left\{ \ln \left| \frac{q}{\Lambda_{\text{PV}}} \right| + \sum_{k=1}^{N_{\text{PV}}} \left[\frac{1}{2} \ln \left(\frac{M_k^2}{\Lambda_{\text{PV}}^2} \right) + \sqrt{1 + \frac{4M_k^2}{q^2}} \operatorname{arcoth} \left(\sqrt{1 + \frac{4M_k^2}{q^2}} \right) \right] + \right. \\ \left. - \frac{1}{2q} \left[(2|\mu| + q) \ln \left| \frac{2|\mu| + q}{\Lambda_{\text{PV}}} \right| + (2|\mu| - q) \ln \left| \frac{2|\mu| - q}{\Lambda_{\text{PV}}} \right| \right] + \right. \\ \left. - \sum_{k=1}^{N_{\text{PV}}} \Theta(\bar{\mu}_k^2) \left[-\operatorname{artanh} \left(\frac{\bar{\mu}_k}{|\mu|} \right) + \frac{1}{2} \sqrt{1 + \frac{4M_k^2}{q^2}} \ln \left| \frac{q|\mu| + \bar{\mu}_k \sqrt{q^2 + 4M_k^2}}{q|\mu| - \bar{\mu}_k \sqrt{q^2 + 4M_k^2}} \right| - \frac{|\mu|}{q} \ln \left| \frac{2\bar{\mu}_k + q}{2\bar{\mu}_k - q} \right| \right] \right\}. \quad (\text{C12})$$

In the limit of vanishing external momentum q , one obtains

$$L_{2,\phi_i}(q = 0, \bar{\sigma}, \mu, T) = -\frac{\delta_{i,0} 4\bar{\sigma}^2}{(4\pi)^2} \sum_{k=0}^{N_{\text{PV}}} c_k \left\{ \frac{1}{2} \ln \left(\frac{M_k^2}{\Lambda_{\text{PV}}^2} \right) - \int_0^\infty dp \frac{n(E_k) + \bar{n}(E_k)}{E_k} \right\} \quad (\text{C13})$$

and in the zero temperature limit one has

$$L_{2,\phi_i}(q = 0, \bar{\sigma}, \mu, T = 0) = -\frac{\delta_{i,0} 4\bar{\sigma}^2}{(4\pi)^2} \sum_{k=0}^{N_{\text{PV}}} c_k \left\{ \frac{1}{2} \ln \left(\frac{M_k^2}{\Lambda_{\text{PV}}^2} \right) - \Theta(\bar{\mu}_k^2) \operatorname{arsinh} \left(\frac{\bar{\mu}_k}{|\bar{\sigma}|} \right) \right\} \quad (\text{C14})$$

in consistency with the zero q limit of Eq. (C11). Taking $q = \bar{\sigma} = 0$, one obtains from Eq. (C9)

$$L_{2,\phi_i}(q = 0, \bar{\sigma} = 0, \mu, T) = 0. \quad (\text{C15})$$

2. Spatial Momentum Cutoff

a. The Momentum Independent Integral l_1

For the SC scheme, one finds

$$l_1(\bar{\sigma}, \mu, T) = \frac{1}{8\pi^2} \left\{ \Lambda_{\text{SC}} \sqrt{\bar{\sigma}^2 + \Lambda_{\text{SC}}^2} - \operatorname{arsinh} \left(\frac{\Lambda_{\text{SC}}}{|\bar{\sigma}|} \right) \bar{\sigma}^2 - \int_0^{\Lambda_{\text{SC}}} dp p^2 \frac{n(E) + \bar{n}(E)}{E} \right\}, \quad (\text{C16})$$

which contains the vacuum contribution

$$l_1(\bar{\sigma}, \mu = 0, T = 0) = \frac{1}{8\pi^2} \left\{ \Lambda_{\text{SC}} \sqrt{\bar{\sigma}^2 + \Lambda_{\text{SC}}^2} - \operatorname{arsinh} \left(\frac{\Lambda_{\text{SC}}}{|\bar{\sigma}|} \right) \bar{\sigma}^2 \right\}. \quad (\text{C17})$$

For $\bar{\sigma} = T = \mu = 0$ one has

$$l_1(\bar{\sigma} = 0, \mu = 0, T = 0) = \frac{\Lambda_{\text{SC}}^2}{8\pi^2}. \quad (\text{C18})$$

At zero temperature, one can give a closed form expression

$$\begin{aligned} l_1(\bar{\sigma}, \mu, T = 0) &= \frac{1}{8\pi^2} \left\{ \Lambda_{\text{SC}} \sqrt{\bar{\sigma}^2 + \Lambda_{\text{SC}}^2} - \operatorname{arsinh} \left(\frac{\Lambda_{\text{SC}}}{|\bar{\sigma}|} \right) \bar{\sigma}^2 - \int_0^{\Lambda_{\text{SC}}} dp \frac{p^2}{E} \Theta(\mu^2 - E^2) \right\} = \\ &= \frac{1}{8\pi^2} \left\{ \Lambda_{\text{SC}} \sqrt{\bar{\sigma}^2 + \Lambda_{\text{SC}}^2} - \operatorname{arsinh} \left(\frac{\Lambda_{\text{SC}}}{|\bar{\sigma}|} \right) \bar{\sigma}^2 + \right. \\ &\quad \left. - \Theta(\bar{\mu}^2) \left[P \sqrt{\bar{\sigma}^2 + P^2} - \operatorname{arsinh} \left(\frac{P}{|\bar{\sigma}|} \right) \bar{\sigma}^2 \right]^{P=\min(\Lambda_{\text{SC}}, \bar{\mu})} \right\} = \\ &= \frac{1}{8\pi^2} \begin{cases} \Lambda_{\text{SC}} \sqrt{\bar{\sigma}^2 + \Lambda_{\text{SC}}^2} - \operatorname{arsinh} \left(\frac{\Lambda_{\text{SC}}}{|\bar{\sigma}|} \right) \bar{\sigma}^2 & \text{if } \bar{\mu}^2 = 0, \\ \Lambda_{\text{SC}} \sqrt{\bar{\sigma}^2 + \Lambda_{\text{SC}}^2} - \operatorname{arsinh} \left(\frac{\Lambda_{\text{SC}}}{|\bar{\sigma}|} \right) \bar{\sigma}^2 - \bar{\mu}|\mu| + \operatorname{arsinh} \left(\frac{\bar{\mu}}{|\bar{\sigma}|} \right) \bar{\sigma}^2 & \text{if } 0 < \bar{\mu}^2 < \Lambda_{\text{SC}}^2, \\ 0 & \text{if } \bar{\mu}^2 > \Lambda_{\text{SC}}^2 \end{cases} \quad (\text{C19}) \end{aligned}$$

and in the limit of vanishing $\bar{\sigma}$

$$l_1(\bar{\sigma} = 0, \mu, T = 0) = \frac{1}{8\pi^2} \left\{ \Lambda_{\text{SC}}^2 - \Theta(\mu^2) \left[P^2 \right]^{P=\min(\Lambda_{\text{SC}}, |\mu|)} \right\} = \quad (\text{C20})$$

$$= \frac{1}{8\pi^2} \begin{cases} \Lambda_{\text{SC}}^2 & \text{if } \mu^2 = 0, \\ \Lambda_{\text{SC}}^2 - \mu^2 & \text{if } 0 < \mu^2 < \Lambda_{\text{SC}}^2, \\ 0 & \text{if } \mu^2 > \Lambda_{\text{SC}}^2. \end{cases} \quad (\text{C21})$$

b. The Momentum Dependent Integral l_2

The evaluation of L_2 differs from the PV scheme significantly, because shifts in the momentum integral would shift the integration bound Λ_{SC} . One finds

$$\begin{aligned} L_{2, \phi_i}(q, \bar{\sigma}, \mu, T = 0) &= \frac{1}{(2\pi)^2} \int_0^{\Lambda_{\text{SC}}} dp p^2 \int_0^\pi d\theta \sin \theta \frac{pq \cos \theta + q^2 + 2\delta_{i,0} \bar{\sigma}^2}{2pq \cos \theta + q^2} \times \\ &\quad \times \left[\frac{1 - n(E) - \bar{n}(E)}{2E} - \frac{1 - n(E_{\mathbf{p}+\mathbf{q}}) - \bar{n}(E_{\mathbf{p}+\mathbf{q}})}{2E_{\mathbf{p}+\mathbf{q}}} \right] = \end{aligned}$$

$$\begin{aligned}
&= \frac{1}{8\pi^2} \int_0^{\Lambda_{\text{SC}}} dp p \left\{ \frac{\Theta(E^2 - \mu^2)}{E} \left[\frac{q^2 + \delta_{i,0} 4\bar{\sigma}^2}{4q} \ln \left(\left| \frac{q+2p}{q-2p} \right| \right) + p \right] + \right. \\
&\quad + \Theta(E_{p+q}^2 - \mu^2) \left[\frac{-1}{2q} \left\{ \begin{array}{ll} (E_{p+q} - \mu) & \text{if } \mu^2 \geq E_{p-q}^2 \\ (E_{p+q} - E_{p-q}) & \text{otherwise} \end{array} \right\} + \right. \\
&\quad \left. \left. + \frac{q^2 + \delta_{i,0} 4\bar{\sigma}^2}{4qE} \left\{ \begin{array}{ll} \ln \left| \frac{\mu^2 - E^2}{2pq+q^2} \frac{(E_{p+q}+E)^2}{(|\mu|+E)^2} \right| & \text{if } \mu^2 \geq E_{p-q}^2 \\ \ln \left| \frac{2p-q}{2p+q} \frac{(E_{p+q}+E)^2}{(E_{p-q}+E)^2} \right| & \text{otherwise} \end{array} \right\} \right] \right\}. \tag{C22}
\end{aligned}$$

At zero temperature, this yields

$$\begin{aligned}
&L_{2,\phi_i}(q, \bar{\sigma}, \mu, T=0) = \\
&= \frac{1}{8\pi^2} \left[(q^2 + \delta_{i,0} 4\bar{\sigma}^2) \left(\frac{E}{4q} \ln \left| \frac{2p+q}{2p-q} \right| + \frac{1}{8} \ln \left| \frac{p+E}{p-E} \right| - \frac{\sqrt{4\bar{\sigma}^2+q^2}}{8q} \ln \left| \frac{qE+p\sqrt{4\bar{\sigma}^2+q^2}}{qE-p\sqrt{4\bar{\sigma}^2+q^2}} \right| \right) + \right. \\
&\quad \left. - \frac{1}{2} (pE - \bar{\sigma}^2 \ln |\bar{\sigma}p + \bar{\sigma}E|) \right]_{p=P_{L,0}}^{p=\Lambda_{\text{SC}}} + \\
&\quad + \frac{1}{8\pi^2} \left[\frac{1}{2q} \left\{ \begin{array}{ll} -\frac{q\bar{\sigma}^2 \operatorname{arsinh}(\frac{p+q}{|\bar{\sigma}|}) + q(p+q)E_{p+q}}{2} - \frac{\mu p^2}{2} + \frac{E_{p+q}^3}{3} & \text{if } \mu^2 \geq E_{p-q}^2 \\ -\frac{q\bar{\sigma}^2}{2} \left[\operatorname{arsinh} \left(\frac{p+q}{|\bar{\sigma}|} \right) + \operatorname{arsinh} \left(\frac{p-q}{|\bar{\sigma}|} \right) \right] + \\ + \frac{2p^2 - q^2 + 2\bar{\sigma}^2}{6} (E_{p+q} - E_{p-q}) + \frac{qE}{6} (E_{p+q} + E_{p-q}) & \text{otherwise} \end{array} \right\} + \right. \\
&\quad \left. + \frac{q^2 + \delta_{i,0} 4\bar{\sigma}^2}{4} \times \right. \\
&\quad \times \left. \left\{ \begin{array}{ll} 0 & \text{if } \mu^2 \geq E_{p-q}^2 \\ \operatorname{artanh} \left(\frac{p}{E} \right) + \frac{E}{q} \ln \left| \frac{2p-q}{2p+q} \right| + \frac{\sqrt{q^2+4\bar{\sigma}^2}}{2q} \ln \left| \frac{qE+\sqrt{q^2+4\bar{\sigma}^2}p}{qE-\sqrt{q^2+4\bar{\sigma}^2}p} \right| & \text{otherwise} \end{array} \right\} \right]_{p=P_{L,q}}^{p=\Lambda_{\text{SC}}} + \\
&\quad + \frac{1}{8\pi^2} \int_{P_{L,q}}^{\Lambda_{\text{SC}}} dp p \frac{q^2 + \delta_{i,0} 4\bar{\sigma}^2}{E4q} \left\{ \begin{array}{ll} \ln \left| \frac{\mu^2 - E^2}{2pq+q^2} \frac{(E_{p+q}+E)^2}{(|\mu|+E)^2} \right| & \text{if } \mu^2 \geq E_{p-q}^2 \\ \ln \left(\frac{(E_{p+q}+E)^2}{(E_{p-q}+E)^2} \right) & \text{otherwise} \end{array} \right\} \tag{C23}
\end{aligned}$$

and for $\bar{\sigma} = 0$

$$\begin{aligned}
&L_{2,\phi_i}(q, \bar{\sigma} = 0, \mu, T=0) = \\
&= \frac{1}{8\pi^2} \left[\frac{q}{8} f(2p, q) + 4p^2 \right]_{p=|\mu|}^{p=\Lambda_{\text{SC}}} + \\
&\quad - \frac{1}{16\pi^2 q} \left[\left\{ \begin{array}{ll} \frac{2}{3} p^3 & \text{if } p \leq q - |\mu| \\ \frac{p^3}{3} + \frac{p^2}{2} (|\mu| + q) - \frac{(|\mu|-q)^2 (5|\mu|+q)}{6} & \text{if } q - |\mu| < p < q + |\mu| \\ p^2 q + 3\mu^2 q - \frac{q^3}{3} & \text{if } p \geq q + |\mu| \end{array} \right\} \right]_{p=\max(0, \mu-q)}^{p=\Lambda_{\text{SC}}} + \tag{C24}
\end{aligned}$$

$$\left. \begin{aligned}
& \frac{1}{2} [f(2p, q) - 4p (\ln q + 1)] && \text{if } p \leq q - |\mu|, \\
& \frac{q \ln |2p+q|}{2} - f(p, |\mu|) + p \left(\ln \left(\frac{2p+q}{q} \right) - 1 \right) + \\
& + \frac{1}{2} [f(2(q - |\mu|), q) - 4(q - |\mu|) (\ln q + 1)] + \\
& - \frac{q \ln |3q-|\mu||}{2} + f(q - |\mu|, |\mu|) - (q - |\mu|) \left(\ln \left(\frac{3q-|\mu|}{q} \right) - 1 \right) && \text{if } q - |\mu| < p < q + |\mu|, \\
& \frac{f(2p, q)}{2} - \frac{f(2(q+|\mu|), q)}{2} \\
& + \frac{1}{2} [f(2(q - |\mu|), q) - 4(q - |\mu|) (\ln q + 1)] + \\
& + \frac{q \ln |3q+|\mu||}{2} - f(q + |\mu|, \mu) + (q + |\mu|) \left(\ln \left(\frac{3q+|\mu|}{q} \right) - 1 \right) + \\
& - \frac{q \ln |3q-|\mu||}{2} + f(q - |\mu|, |\mu|) - (q - |\mu|) \left(\ln \left(\frac{3q-|\mu|}{q} \right) - 1 \right) && \text{if } p \geq q + |\mu|
\end{aligned} \right\} \begin{array}{l} p=\Lambda_{\text{SC}} \\ \\ \\ \\ \\ \\ \\ p=\max(0, \mu-q) \end{array},$$

where we defined

$$f(x, y) = (x + y) \ln|x + y| - (x - y) \ln|x - y|. \quad (\text{C25})$$

3. Lattice Regularization

For the lattice regulations, one cannot split up $\Gamma^{(2)}$ according to Eq. (C1). Instead, one needs to evaluate

$$\begin{aligned}
\ell_{3, \phi_i}(\mathbf{p}, q, \bar{\sigma}, \mu) &= \int_{-\Lambda_{\text{LFT}}}^{\Lambda_{\text{LFT}}} \frac{dp_0}{2\pi} \text{tr} [c_i S_X(p + (0, \mathbf{q})) c_i S_X(p)] = \\
&= \frac{\bar{N}}{\sum_{i=1}^3 \left(\mathcal{P}_X^2(\mathbf{p}_i) - \mathcal{P}_X^2(\mathbf{p}_i + \mathbf{q}_i) \right)} \times \\
&\times \left[\frac{E^2 - \sum_{i=1}^3 \mathcal{P}_X(\mathbf{p}_i + \mathbf{q}_i) \mathcal{P}_X(\mathbf{p}_i) + \bar{\sigma}^2}{E} \left[\arctan \left(\frac{\Lambda_{\text{LFT}}}{E - |\mu|} \right) + \arctan \left(\frac{\Lambda_{\text{LFT}}}{E + |\mu|} \right) \right] + \right. \\
&\left. - \frac{E_{\mathbf{p}+\mathbf{q}}^2 - \sum_{i=1}^3 \mathcal{P}_X(\mathbf{p}_i + \mathbf{q}_i) \mathcal{P}_X(\mathbf{p}_i) + \bar{\sigma}^2}{E_{\mathbf{p}+\mathbf{q}}} \left[\arctan \left(\frac{\Lambda_{\text{LFT}}}{E_{\mathbf{p}+\mathbf{q}} - |\mu|} \right) + \arctan \left(\frac{\Lambda_{\text{LFT}}}{E_{\mathbf{p}+\mathbf{q}} + |\mu|} \right) \right] \right],
\end{aligned} \quad (\text{C26})$$

with the lattice dispersion relations $\mathcal{P}_{\text{SLAC}}$ and $\mathcal{P}_{\text{Hybrid}}$ given in Eq. (17) and Eq. (A8), respectively, and $\vec{c} = (\mathbf{1}, i\gamma_5\tau_3)$. The energy E is defined as in Eq. (A7) and

$$E_{\mathbf{p}+\mathbf{q}} = \sqrt{\sum_{i=1}^3 \mathcal{P}_X^2(p_i + q_i) + \bar{\sigma}^2}. \quad (\text{C27})$$

The contribution of ℓ_{3, ϕ_i} to $\Gamma_{\phi_i}^{(2)}$ depends on the chosen lattice discretization and is given below.

a. SLAC Fermions

For the SLAC discretization, the bosonic two-point function is then given by

$$\Gamma_{\phi_i}^{(2)}(q, \bar{\sigma}, \mu, T = 0) = \frac{1}{2G} - \frac{1}{2\pi} \int_{-\Lambda_{\text{LFT}}}^{\Lambda_{\text{LFT}}} \frac{dp_1}{2\pi} \int_{-\Lambda_{\text{LFT}}}^{\Lambda_{\text{LFT}}} \frac{dp_2}{2\pi} \int_{-\Lambda_{\text{LFT}}}^{\Lambda_{\text{LFT}}} \frac{dp_3}{2\pi} \ell_{3, \phi_i}(\mathbf{p}, q, \bar{\sigma}^2, \mu). \quad (\text{C28})$$

b. Hybrid Fermions

For the Hybrid discretization, the bosonic two-point function is then given by

$$\Gamma_{\phi_i}^{(2)}(q, \bar{\sigma}, \mu, T=0) = \frac{1}{2G} - \tilde{W}_X(\mathbf{q}) \tilde{W}_X(-\mathbf{q}) \frac{1}{2\pi} \int_{-\Lambda_{\text{LFT}}}^{\Lambda_{\text{LFT}}} \frac{dp_1}{2\pi} \int_{-\Lambda_{\text{LFT}}}^{\Lambda_{\text{LFT}}} \frac{dp_2}{2\pi} \int_{-\Lambda_{\text{LFT}}}^{\Lambda_{\text{LFT}}} \frac{dp_3}{2\pi} \ell_{3,\phi_i}(\mathbf{p}, q, \bar{\sigma}^2, \mu) \quad (\text{C29})$$

with the weighting function \tilde{W} as introduced in Section II C 3 b.

Appendix D: Formulas for the Wave-Function Renormalization

According to Eq. (10), we perform a double derivative of $\Gamma_{\phi_i}^{(2)}$ with respect to q and take the limit $q \rightarrow 0$ in order to obtain z_{ϕ_i} .

1. Pauli-Villars

For the PV scheme, this amounts to

$$\begin{aligned} z_{\phi_i}(\bar{\sigma}, \mu, T) = & \\ = \frac{\bar{N}}{16\pi^2} \sum_{k=0}^{N_{\text{PV}}} c_k & \left\{ -\frac{1}{3} \frac{\delta_{i,0} \bar{\sigma}^2}{M_k^2} - \frac{1}{2} \ln \left(\frac{M_k^2}{\Lambda_{\text{PV}}^2} \right) - \int_0^\infty dp \frac{n(E_k) + \bar{n}(E_k)}{E_k} + \right. \\ & \left. - \frac{\bar{\sigma}^2}{3} \int_0^\infty dp \frac{1}{E_k^3} \left[-n(E_k) - \bar{n}(E_k) + \frac{E_k}{T} \left[n^2(E_k) + \bar{n}^2(E_k) - n(E_k) - \bar{n}(E_k) \right] \right] \right\} \end{aligned} \quad (\text{D1})$$

and at zero temperature, this gives

$$\begin{aligned} z_{\phi_i}(\bar{\sigma}, \mu, T=0) = & \\ = \frac{\bar{N}}{16\pi^2} \sum_{k=0}^{N_{\text{PV}}} c_k & \left\{ -\frac{1}{3} \frac{\delta_{i,0} \bar{\sigma}^2}{M_k^2} - \frac{1}{2} \ln \left(\frac{M_k^2}{\Lambda_{\text{PV}}^2} \right) + \right. \\ & \left. - \int_0^\infty dp \frac{\Theta(\mu^2 - E_k^2)}{E_k} - \frac{\bar{\sigma}^2}{3} \int_0^\infty dp \frac{1}{E_k^3} \left[\Theta(\mu^2 - E_k^2) + \frac{E_k}{|\mu|} \delta \left(\frac{E_k}{\mu} - 1 \right) \right] \right\} = \\ = \frac{\bar{N}}{16\pi^2} \sum_{k=0}^{N_{\text{PV}}} c_k & \left\{ -\frac{1}{3} \frac{\delta_{i,0} \bar{\sigma}^2}{M_k^2} - \frac{1}{2} \ln \left(\frac{M_k^2}{\Lambda_{\text{PV}}^2} \right) - \frac{\Theta(\bar{\mu}_k^2)}{3} \left[3 \operatorname{arsinh} \left(\frac{\bar{\mu}_k}{M_k} \right) + \frac{\bar{\sigma}^2}{M_k^2} \left| \frac{\bar{\mu}_k}{\mu} \right| + \frac{\bar{\sigma}^2}{\mu \bar{\mu}_k} \right] \right\}. \end{aligned} \quad (\text{D2})$$

Evaluating Eq. (D1) for $\bar{\sigma} = 0$ gives

$$\begin{aligned} z_{\phi_i}(\bar{\sigma} = 0, \mu, T) = & \\ = \frac{\bar{N}}{16\pi^2} & \left\{ \int_0^\infty dp \frac{1}{p} \left[1 - n(p) - \bar{n}(p) + \frac{p}{T} \left(n^2(p) + \bar{n}^2(p) - n(p) - \bar{n}(p) \right) \right] + \right. \\ & \left. + \sum_{k=1}^{N_{\text{PV}}} c_k \int_0^\infty dp \frac{p^2}{E_k^3} \left[1 - n(E_k) - \bar{n}(E_k) + \frac{E_k}{T} \left(n^2(E_k) + \bar{n}^2(E_k) - n(E_k) - \bar{n}(E_k) \right) \right] \right\} \end{aligned} \quad (\text{D3})$$

and for $\bar{\sigma} = T = 0$

$$\begin{aligned} z_{\phi_i}(\bar{\sigma} = 0, \mu \neq 0, T = 0) = & \\ = \frac{\bar{N}}{16\pi^2} & \left\{ \frac{1}{2} \ln(4) - \frac{1}{3} - \frac{\delta_{i,0}}{3} - \frac{1}{2} \ln \left(\frac{\mu^2}{\Lambda_{\text{PV}}^2} \right) + \right. \\ & \left. + \sum_{k=1}^{N_{\text{PV}}} c_k \left[-\frac{1}{3} \frac{\delta_{i,0} \bar{\sigma}^2}{M_k^2} - \frac{1}{2} \ln \left(\frac{M_k^2}{\Lambda_{\text{PV}}^2} \right) - \frac{\Theta(\bar{\mu}_k^2)}{3} \left[3 \operatorname{arsinh} \left(\frac{\bar{\mu}_k}{M_k} \right) + \frac{\bar{\sigma}^2}{M_k^2} \left| \frac{\bar{\mu}_k}{\mu} \right| + \frac{\bar{\sigma}^2}{\mu \bar{\mu}_k} \right] \right] \right\}. \end{aligned} \quad (\text{D4})$$

2. Spatial Momentum Cutoff

In the SC scheme, one finds

$$\begin{aligned}
z_{\phi_i}(\bar{\sigma}, \mu, T) &= \\
&= \frac{\bar{N}}{16\pi^2} \left\{ 2 \int_0^{\Lambda_{\text{SC}}} dp p^2 \frac{1}{E^3} \left[1 - n(E) - \bar{n}(E) + \frac{E}{T} (n^2(E) + \bar{n}^2(E) - n(E) - \bar{n}(E)) \right] + \right. \\
&\quad - 3 \int_0^{\Lambda_{\text{SC}}} dp \frac{\delta_{i,0} \bar{\sigma}^2 p^2 + \frac{p^4}{3}}{E^5} \left[1 - n(E) - \bar{n}(E) + \frac{E}{T} [n^2(E) + \bar{n}^2(E) - n(E) - \bar{n}(E)] + \right. \\
&\quad \quad \left. \left. - \frac{E^2}{3T^2} [2n^3(E) + 2\bar{n}^3(E) - 3n^2(E) - 3\bar{n}^2(E) + n(E) + \bar{n}(E)] \right] + \right. \\
&\quad + \frac{\delta_{i,0}}{3} \int_0^{\Lambda_{\text{SC}}} dp \frac{5\bar{\sigma}^2 p^4}{E^7} \left[1 - n(E) - \bar{n}(E) + \frac{E}{T} [n^2(E) + \bar{n}^2(E) - n(E) - \bar{n}(E)] + \right. \\
&\quad \quad - \frac{2E^2}{15T^2} [2n^3(E) + 2\bar{n}^3(E) - 3n^2(E) - 3\bar{n}^2(E) + n(E) + \bar{n}(E)] + \\
&\quad \quad \left. \left. + \frac{E^3}{15T^3} [6n^4(E) + 6\bar{n}^4(E) - 12n^3(E) - 12\bar{n}^3(E) + 7n^2(E) + 7\bar{n}^2(E) - n(E) - \bar{n}(E)] \right] \right\}. \tag{D5}
\end{aligned}$$

Note that the higher orders of distribution functions compared to the PV results stems from the fact that partial integration was not performed because the boundary terms would be non-vanishing. For $\bar{\sigma} = 0$ one finds

$$\begin{aligned}
z_{\phi_i}(\bar{\sigma} = 0, \mu, T) &= \\
&= \frac{\bar{N}}{16\pi^2} \left\{ \int_0^{\Lambda_{\text{SC}}} dp \frac{1}{p} \left[1 - n(p) - \bar{n}(p) + \frac{p}{T} [n^2(p) + \bar{n}^2(p) - n(p) - \bar{n}(p)] \right] + \right. \\
&\quad \left. + \int_0^{\Lambda_{\text{SC}}} dp \frac{p}{3T^2} [2n^3(p) + 2\bar{n}^3(p) - 3n^2(p) - 3\bar{n}^2(p) + n(p) + \bar{n}(p)] \right\}. \tag{D6}
\end{aligned}$$